

## An investigation of the Ni/carbonate interfaces on dual function materials in integrated CO<sub>2</sub> capture and utilisation cycles



Xianyue Wu <sup>a,c,d</sup>, Ribooga Chang <sup>b</sup>, Mingwu Tan <sup>a,e</sup>, Longgang Tao <sup>a,e</sup>, Qianwenhao Fan <sup>a</sup>, Xiaochun Hu <sup>a</sup>, Hui Ling Tan <sup>a,d</sup>, Michelle Åhlén <sup>b</sup>, Ocean Cheung <sup>b,\*</sup>, Wen Liu <sup>a,\*</sup>

<sup>a</sup> School of Chemistry, Chemical Engineering and Biotechnology, Nanyang Technological University, 62 Nanyang Drive, 637459, Singapore

<sup>b</sup> Nanotechnology and Functional Materials, Department of Materials Science and Engineering, Uppsala University, SE75121, Sweden

<sup>c</sup> Nanyang Environment And Water Research Institute (NEWRI), 1 Cleantech Loop, 637141, Singapore

<sup>d</sup> The Cambridge Centre for Advanced Research and Education (CARES), 1 Create WayCREATE Tower, #05-05, 138602, Singapore

<sup>e</sup> Institute of Sustainability for chemicals, Energy and Environment, Agency for Science, Technology and Research (A\*STAR), 1 Pesek Road, Jurong Island, 627833, Singapore

### ARTICLE INFO

#### Keywords:

CO<sub>2</sub> capture and utilization  
CO<sub>2</sub> hydrogenation  
Dual function material  
In situ, characterization

### ABSTRACT

CO<sub>2</sub> capture and utilisation (CCU) is a promising strategy to effectively mitigate the adverse greenhouse effects caused by CO<sub>2</sub> emissions at an industrial scale. Through a process intensification strategy known as integrated CO<sub>2</sub> capture and utilisation (ICCU), CO<sub>2</sub> capture and catalytic CO<sub>2</sub> conversion can be achieved in a single process with the use of dual function materials (DFMs), which are both CO<sub>2</sub> sorbents and CO<sub>2</sub> conversion catalysts. Given the significantly different operating conditions of ICCU from conventional catalytic CO<sub>2</sub> hydrogenation, the catalytic mechanism of DFMs, especially during CO<sub>2</sub> hydrogenation, needs to be thoroughly investigated. In this study, the relationship between the nature of the Ni/carbonate interfaces and the performance of Ni-based DFMs over ICCU cycles is systematically investigated. A series of Ni/alkaline earth carbonate DFMs were synthesised with varying Ca:Mg ratios to simulate different metal-carbonate model interfaces. At 400 °C, CH<sub>4</sub> formation with nearly 100% CH<sub>4</sub> selectivity was achieved on Ni/CaCO<sub>3</sub> over 15 ICCU cycles. In general, Ni/CaCO<sub>3</sub> interfaces correspond to higher CO<sub>2</sub> conversion and higher CH<sub>4</sub> selectivity than Ni/MgCO<sub>3</sub> interfaces. Such trend may be attributed to the higher surface basicity of CaO and the higher thermal stability of CaCO<sub>3</sub>. As a consequence, the hydrogenation of the Ni/CaCO<sub>3</sub> interface proceed via the formate pathway, in which carbonates are consecutively converted to surface formates, methoxyl, methyl species and eventually desorb as methane. This reaction model is applicable to the hydrogenation of both surface carbonate and bulk carbonates, although the former proceeds with much faster kinetics. On the weakly alkaline Ni/MgCO<sub>3</sub> interface, MgCO<sub>3</sub> preferentially decomposes to form gaseous CO<sub>2</sub>, which is subsequently hydrogenated via the reverse-water-gas-shift pathway, with CO as the key reaction intermediate. Interestingly, in situ infrared spectroscopy shows similar surface significant species during the direct hydrogenation of DFMs and during the conventional catalytic hydrogenation of molecular CO<sub>2</sub>, suggesting that the catalytic mechanisms during the two operating regimes are highly correlated.

### 1. Introduction

With the rapid urbanization and industrialization, the release of CO<sub>2</sub> has been dramatically increasing, e.g. from 20.5 Gt in 1990 to 36.9 Gt in 2022. [1,2] A large amount of CO<sub>2</sub> emissions and the resulting greenhouse effects, e.g., climate change, have posed an existential threat to the modern civilisation. Well-known consequences of climate change include rising sea level, [3] more frequent and destructive hurricanes,

[4] flooding, [5] etc. Hence, it is important and urgent to efficiently control and mitigate anthropogenic CO<sub>2</sub> emissions. The carbon capture and utilisation (CCU) scheme has been proposed to prevent the release of CO<sub>2</sub> and convert the captured CO<sub>2</sub> to fuels and chemicals that are conventionally derived from fossil fuels. Therefore, CCU has the potential to facilitate the transition to a defossilised economy. [6].

CCU involves firstly capturing CO<sub>2</sub> from emission sources, usually the combustion of fossil fuels (i.e., post-combustion capture). This can

\* Corresponding authors.

E-mail addresses: [ocean.cheung@angstrom.uu.se](mailto:ocean.cheung@angstrom.uu.se) (O. Cheung), [wenliu@ntu.edu.sg](mailto:wenliu@ntu.edu.sg) (W. Liu).

be achieved by scrubbing CO<sub>2</sub> from combustion flue gases using liquid amine solutions [7] or solid sorbents that are either highly porous [8–11] or suitably alkaline. [12] In particular, oxides of alkali metals or alkaline earth metals, e.g., CaO, [13,14] MgO, [15] Na<sub>2</sub>O, [16] Na<sub>2</sub>CO<sub>3</sub>, [17,18] and Li-Al-oxides, [19] exhibit high CO<sub>2</sub> uptake capacities, fast uptake kinetics, low costs and high earth-abundance. [20] The captured CO<sub>2</sub> can be directly utilised for carbonating building materials, [21] filling fire extinguishers [22] and enhanced oil recovery (CO<sub>2</sub>-EOR), [23] or catalytically converted to valuable products, [24,25] e.g., by hydrogenation using green hydrogen [26] to produce methane (methanation), CO (reverse water-gas-shift reaction), alcohols or long-chain hydrocarbons (Fischer-Tropsch synthesis). [27–30] The fuels and chemicals produced by CCU can also be considered as carriers storing the intermittently available renewable energy. [31] Therefore, CCU presents an opportunity to transition from a fossil-based chemical industry to an renewable one. [32].

In recent years, an integrated CO<sub>2</sub> capture and utilisation (ICCU) scheme, which achieves CO<sub>2</sub> capture and CO<sub>2</sub> conversion in a single reactor system, emerges as a unique process intensification approach for CCU. [33–36] During ICCU, the endothermic sorbent regeneration and the exothermic CO<sub>2</sub> hydrogenation reactions were achieved in a single step, thereby simplifying the process while saving energy. Doing so requires the availability of a dual function material (DFM) that is both a sorbent and a catalyst. [37] Intuitively, most designs of DFMs involve interfacing a catalytically active metal (for CO<sub>2</sub> reduction) with a solid CO<sub>2</sub> sorbent (for CO<sub>2</sub> capture). [33,36] Among many catalytic metal sites studied, e.g., Ru, Rh, Ni and Co, [38,39] Ni-based catalysts show satisfactory activity for CO<sub>2</sub> hydrogenation and relatively low costs. [40] Alkali metal oxides and alkaline earth metal oxides, such as Na<sub>2</sub>O, [16, 41–43] LiAlO<sub>2</sub>, [19] MgO [15,44] and CaO [45,46] are commonly employed to provide CO<sub>2</sub> capture functionalities. To further improve the catalytic conversion of the capture CO<sub>2</sub> and the long-term stabilities, the DFMs are promoted by the addition of reducible (e.g., CeO<sub>2</sub>, [47–49] TiO<sub>2</sub>, [50] ZrO<sub>2</sub>, [51–53] etc.) and/or irreducible (e.g., SiO<sub>2</sub>, [54,55] Al<sub>2</sub>O<sub>3</sub>, [56–58] MgO, [44] etc.), respectively. For example, Farrauto et al. [42] supported Ru/Na<sub>2</sub>O DFMs on Al<sub>2</sub>O<sub>3</sub>, achieving stable performance over 50 cycles of ICCU owing to improved sintering resistance.

In recent years, there have been substantial advances in the development of ICCU cycles, including the development of high performance DFMs and more in-depth mechanistic studies of DFMs when employed in various applications of ICCU cycles. [17,37,59–62] On the other hand,

the catalytic mechanism for the direct hydrogenation of immobilised CO<sub>2</sub> (i.e., chemical bond to DFMs), remains inadequately understood. It is conducive that the direct interaction between the active metal sites and carbonated CO<sub>2</sub> sorbents in DFMs plays a critical role during the catalytic hydrogenation, and warrants more investigation. Broadly speaking, two reaction pathways could take place during the hydrogenation of carbonated DFMs: (i) the carbonates thermally decompose, releasing gaseous CO<sub>2</sub>, which is subsequently adsorbed and converted on the active sites through conventional CO<sub>2</sub> hydrogenation mechanisms [63] and (ii) the hydrogen activated on the metal surface migrates to the carbonates, directly converting them to hydrogenated products, which eventually desorbs, [64] as schematically illustrated in Fig. 1. Regardless of the reaction pathway, key mechanistic insights, including (i) the interaction across the metal-carbonate interface, (ii) the roles of surface carbonates versus bulk carbonates, (iii) the reaction mechanism at the metal-carbonate interface, and (iv) the evolution of the metal-/carbonate interfaces over repeated ICCU cycles remain unclear.

To address the knowledge gaps stated above, this study employs model DFM structures consisting of Ni nanoparticles supported on a nanostructured, highly mesoporous MgCO<sub>3</sub>, CaCO<sub>3</sub>, or a mixture of both, [65–67] to investigate the hydrogenation of the captured CO<sub>2</sub>, either in carbonate form or in gaseous form, during ICCU over the temperature range of 300–400 °C, where both CO<sub>2</sub> methanation and RWGS are thermodynamically favourable. Here, MgCO<sub>3</sub> and CaCO<sub>3</sub> represents two types of surface basicity and decomposition temperatures, [68–70] where are their mixtures are anticipated to possess properties that are in-between the two pure carbonates. The high mesoporosity of the carbonate support would facilitate the uniform dispersion of the Ni nanoparticles in the DFMs. By characterising the Ni/carbonate interfaces using gas adsorption/desorption experiments, electron microscopy and in situ infrared spectroscopy, the relationship between DFM structures, surface properties, catalytic pathways, reaction mechanisms, CO<sub>2</sub> conversion and selectivity are examined and elucidated. Lastly, through a comparative study, the analogy between the structural-functional relationship for DFMs over ICCU cycles and conventional CO<sub>2</sub> hydrogenation reactions is investigated.

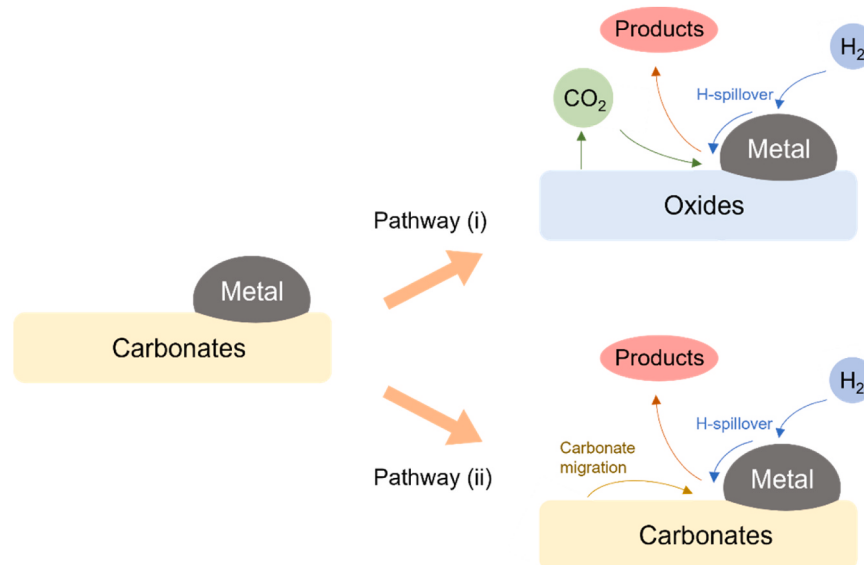


**Fig. 1.** Two possible reaction pathways of catalytic hydrogenation of immobilised CO<sub>2</sub> on DFMs during ICCU cycles.

## 2. Experimental

### 2.1. Materials

Calcium carbonate (CaO, 96–100.5%, FCC grade), magnesium oxide (MgO, 98.0–100.5%), nickel(II) acetate tetrahydrate (98%), citric acid (>99.5%) and ethanolamine ( $\geq 98\%$ ) were purchased from Sigma-Aldrich, USA. Methanol (99.9% high-performance liquid chromatography grade) and ethanol absolute (99.96%) were purchased from VWR International, Sweden. All chemicals were directly used without further purification.

### 2.2. Catalyst preparation

Amorphous calcium carbonate (ACC) and mesoporous magnesium carbonate (MMC) suspensions were synthesized by a sol-gel method via carbonating the corresponding oxides in high-pressure CO<sub>2</sub> atmosphere. [65,67] The obtained ACC and MMC would have high specific surface areas (394–698 m<sup>2</sup>/g) compared to commercial CaCO<sub>3</sub> and MgCO<sub>3</sub> (6.3–18.1 m<sup>2</sup>/g). The NiO/carbonate samples were synthesized by a co-precipitation method, [71] as illustrated in Fig. 2. To make mixtures of MgCO<sub>3</sub> and CaCO<sub>3</sub>, the required amounts of ACC and/or MMC suspensions were mixed. Separately, nickel acetate was dissolved in methanol to obtain a clear solution. Then, the nickel acetate solution was added to the mixed suspension. The formed mixture was stirred for 30 min, which allowed the deposition of the NiO precursors onto the carbonate substrates. Afterwards, ethanolamine was added as the stabiliser, while the mixture was left for a further 5 min. To evaporate methanol, the mixture was heated at 150 °C for 1 h, and then dried at 250 °C in air for 20 h to receive fresh DFM, which primarily consisted of NiO supported on mesoporous carbonates. The loading of NiO in each fresh DFM was also verified by inductively coupled plasma atomic emission spectrometry (ICP-AES). Prior to reaction, the fresh DFM were reduced in 10 vol% H<sub>2</sub>/N<sub>2</sub> gas at 400 °C for 2 h to produce Ni/carbonate DFM. Using this method, Ni/carbonate DFM with 5 different ACC:MMC mass ratios (viz. 1:0, 3:1, 1:1, 1:3 and 0:1) were prepared, each with a NiO loading of  $\sim 10$  wt%, and are denoted as Ni/Ca, Ni/Ca3Mg1, Ni/Ca1Mg1, Ni/Ca1Mg3 and Ni/Mg, respectively.

### 2.3. Catalyst characterisation

X-ray diffraction (XRD) was performed on a Bruker D8 Advance diffractometer with a K<sub>β</sub>-filtered Cu K<sub>α</sub> source (40 kV, 40 mA,  $\lambda=0.154$  nm) to determine the change of the phase compositions of the fresh DFM and when they are hydrogenated or spent after ICCU cycles.

The scans were collected continuously between  $2\theta = 5^\circ - 120^\circ$ , with a step size of 0.02° and a scan time of 0.5 s per step. The sample rotation was set at 15 rpm to minimise the effect of preferred orientation.

X-ray photoelectron spectroscopy (XPS) was conducted using a PHI Quantera II Scanning XPS Microprobe with Al K<sub>α</sub> radiation ( $h\nu = 1486.6$  eV) to examine the change in the surface compositions of the DFM over ICCU cycles. Prior to XPS measurements of the fresh, hydrogenated or spent DFM, the samples were pretreated by sputtering with Ar plasma for 30 s to clean the surface and remove the oxidic passivation layers. The binding energies of the XPS spectra were calibrated using a reference C-C 1 s peak (B.E.= 284.6 eV).

The morphology of the DFM (specifically, Ni/Ca, Ni/Ca1Mg1 and Ni/Mg) before and after H<sub>2</sub> reduction were examined using transmission electron microscopy (TEM), performed on a JEOL JEM2010 200 kV transmission electron microscope equipped with Gatan Erlangshen CCD camera for high-resolution image and video recording. Prior to TEM, 5 mg of the sample powders were dispersed in 5 mL absolute ethanol. The mixture underwent a 30-min ultrasonication to achieve a uniform dispersion. 1 drop of the suspension, collected from the top of the suspension, was dripped on a copper grid-supported holey carbon film, which was subsequently dried at 60 °C for 30 min. The average Ni particle sizes were estimated based on the sizes of 10 – 20 Ni particles, sampled from the TEM images using ImageJ software.

The specific surface areas of the fresh, hydrogenated or spent samples were determined by the BET (Brunauer, Emmett and Teller) correlation, based on the N<sub>2</sub> adsorption-desorption isotherms of the samples measured at  $-196$  °C using a Micromeritics 3Flex. The samples were degassed at 150 °C for 24 h on a Micromeritics VacPrep 061 degasser prior to the isotherm measurements.

H<sub>2</sub>-temperature programmed reduction (TPR) was conducted on a Micromeritics AutoChem II 2920 to analyse the reduction behaviour of NiO deposited on carbonate. The H<sub>2</sub>-TPR profiles reflect the extent of interaction between the reduced Ni and the alkaline earth metal oxide (e.g., MgO, CaO or a mixture of both). All gas flowrates, from this point onwards, are reported in standard temperature and pressure conditions (S.T.P), unless otherwise stated. In each measurement, 100 mg of fresh DFM sample was pre-calcined at 900 °C for 1 h under an Ar flow of 50 mL/min to fully decompose all carbonates. Afterwards, the sample was cooled down to 40 °C. Then, the inlet gas was switched to 50 mL/min of 10 vol% H<sub>2</sub>/Ar. Subsequently, the temperature of the sample chamber was set to increase from 40 °C to 900 °C at a constant heating rate of 10 °C/min. The off-gas was analysed on-line by a thermal conductivity detector (TCD) to determine the consumption of H<sub>2</sub>.

CO<sub>2</sub>-temperature programmed desorption (CO<sub>2</sub>-TPD) and is conducted using the same equipment as H<sub>2</sub>-TPR to analyse the basicity of

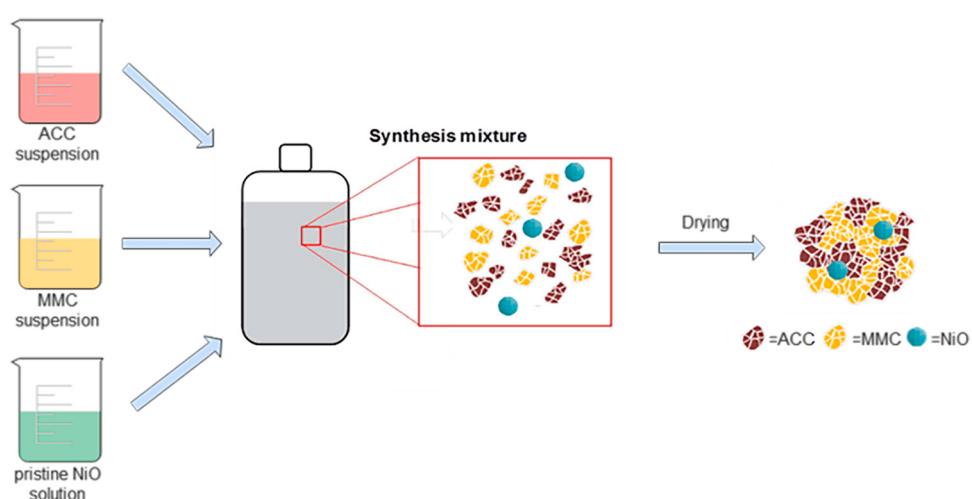


**Fig. 2.** Schematic illustration of the synthesis of fresh DFM consisting of NiO/carbonates. The figure is adapted from [66].

the catalysts. In a typical CO<sub>2</sub>-TPD measurement, 100 mg of fresh DFM sample was pretreated in 10 vol% H<sub>2</sub>/Ar (50 mL/min) at 900 °C to fully decompose all carbonates, while reducing NiO to Ni. The reduced sample was cooled to 30 °C and purged with 50 mL/min of He. The sample was then treated in pure CO<sub>2</sub> (50 mL/min) for 30 min at 40 °C, facilitating saturated CO<sub>2</sub> adsorption. CO<sub>2</sub> desorption was achieved by heating the CO<sub>2</sub>-saturated sample from 40° to 900°C with a heating rate of 10 °C/min, under a flow of pure He (50 mL/min). The amount of CO<sub>2</sub> desorbed was quantified by a TCD analyser. The gas outlet of the CO<sub>2</sub>-TPD measurement was analysed by a mass spectrometer (MS).

CO pulse chemisorption was performed using the same equipment as TPR to measure the surface Ni metal dispersion. The fresh DFM sample (100 mg) was pretreated in 10 vol% H<sub>2</sub>/Ar (50 mL/min) at 400 °C for 1 h and cooled to 40 °C. The reduced sample was then purged with He for 30 min until the TCD signal stabilised. Next, pulses of 10 vol% CO/He (10 mL per each pulse) were injected at 6 min intervals. The pulsed injection was stopped once the samples were saturated and no longer take up any more CO. The total amount of CO adsorbed by the catalysts were subsequently quantified to determine the surface Ni dispersion.

Thermogravimetric analysis (TGA) was carried out on a Mettler-Toledo TGA/DSC. The fresh DFM sample was first dewatered at 150 °C for 30 mins in 50 mL/min N<sub>2</sub>. After the water removal, it was reduced in 50 mL/min of 5 vol% H<sub>2</sub>/N<sub>2</sub> at a heating rate of 5 °C/min from 150° to 900°C. The reduced sample was then cooled to room temperature and subjected to temperature-programmed oxidation (TPO) from room temperature to 900 °C with a heating rate of 5 °C/min in 50 mL/min of air. The TPO results were used to determine the mass fraction of NiO in the sample prior to reduction.

*In situ* diffuse reflectance infrared Fourier transform spectroscopy (*in situ* DRIFTS) was performed using a Bruker Tensor II Fourier-transform spectrometer equipped with a liquid N<sub>2</sub>-cooled MCT (Mercury Cadmium Telluride) detector, fitted with a PIKE Technologies DiffusIR optical accessory and a high temperature (-150 to 1000 °C) PIKE DRIFT environmental cell with ZnSe windows. In a typical measurement, 40 mg of fresh DFM sample consisting of a mixture of KBr and DFMs with a 2:1 mass ratio underwent the following pretreatment steps (1) reduction by 20 mL/min 25 vol% H<sub>2</sub>/Ar for 1 h, (2) purge by 20 mL/min Ar for 15 min, (3) carbonation by 20 mL/min of 25 vol% CO<sub>2</sub>/Ar; all carried out isothermally at 400 °C. Then, two types of DRIFTS experiments were carried out, (i) direct hydrogenation of the Ni/carbonate sample in 25 vol% H<sub>2</sub>/Ar for up to 24 h and (ii) conventional CO<sub>2</sub> methanation in a 5/20/15 mixture of CO<sub>2</sub>/H<sub>2</sub>/Ar (i.e. co-feeding CO<sub>2</sub> and H<sub>2</sub>) with a total flowrate of 40 mL/min for 60 min. Both experiments were conducted isothermally at 400 °C. Throughout the *in situ* DRIFTS experiments, IR spectra were continuously collected over the spectral range of 4000 – 600 cm<sup>-1</sup> wavenumbers with a resolution of 4 cm<sup>-1</sup> and 256 scans per spectrum.

#### 2.4. Direct hydrogenation of Ni/carbonates

The direct hydrogenation experiments were performed in a fixed-bed reactor made of a quartz tube with a length of 50 cm, an inner diameter of 8 mm and a wall thickness of 1 mm. The setup of the reactor system is shown in Fig. S1 in Supporting Information (S.I.). To ensure that the active bed (i.e., where the DFM was located) operated under near-isothermal conditions, the packing arrangement, from bottom to top, was as follows: 1 cm-long rubber stopper, 30 mg silica wool, 25 g inactive Al<sub>2</sub>O<sub>3</sub>, 30 mg silica wool, DFM powders, and 30 mg silica wool. In each experiment, 100 mg of the fresh DFM samples (after pre-reduction in H<sub>2</sub>/N<sub>2</sub> as described in Section 2.2, with size fraction of 0.6–2.0 mm) was loaded into the reactor and heated to 400 °C with a heating rate of 5 °C/min in 100 mL/min of 10 vol% H<sub>2</sub>/N<sub>2</sub>, and then kept isothermal at 400 °C for 1 h to ensure complete reduction of NiO to Ni. The reaction off-gas is analysed by on-line gas analysers (ABB, EL3020) equipped with different detector modules: Uras26 non-dispersive infrared spectrometer (for CH<sub>4</sub>, CO and CO<sub>2</sub>) and Caldos27

thermal conductivity analyser (for H<sub>2</sub>).

#### 2.5. ICCU cycles

The ICCU cycling experiments were conducted by cyclically feeding the packed DFMs with alternating gases of CO<sub>2</sub> and H<sub>2</sub>, analogous to a chemical looping scheme. In each experiment, 100 mg sample (0.6–2.0 mm) was loaded in the quartz fixed bed reactor and calcined at 400 °C in pure N<sub>2</sub> (100 mL/min) for 1 h. Then, the sample was subjected to 15 ICCU cycles, each consisting of the following stages: (1) hydrogenation in 10 vol% H<sub>2</sub>/N<sub>2</sub> (100 mL/min) for 1 h, (2) purge with N<sub>2</sub> (100 mL/min) for 30 min, (3) carbonation in 10 vol% CO<sub>2</sub>/N<sub>2</sub> (100 mL/min) for 1 h, and (4) N<sub>2</sub> purge for 30 min. The temperature was kept isothermal at 400 °C during the ICCU cycles. Because of the focus of the present study is to investigate the Ni/carbonate interface rather than demonstrating high performance DFMs, we chose high space velocities and low DFM loading to facilitate the conversion of carbonates during the hydrogenation stage. As a result, the single-pass conversion of H<sub>2</sub> during the hydrogenation stage and uptake of CO<sub>2</sub> during the carbonation stage are expected to be low. The reaction off-gases are analysed by the same on-line gas analysers as described in Section 2.4.

#### 2.6. Conventional catalytic CO<sub>2</sub> hydrogenation

The performance of the Ni/carbonate DFM for conventional catalytic CO<sub>2</sub> hydrogenation was evaluated using the same apparatus as described in Section 2.4. In each experiment, 100 mg of fresh DFM sample (with a sieve fraction of 0.6–2.0 mm) was loaded into the fixed bed reactor and reduced by 100 mL/min of 10 vol% H<sub>2</sub>/N<sub>2</sub> at 400 °C for 2 h to convert the NiO to Ni metal to form the working catalysts. After reduction, the catalyst was exposed to a 60/15/25 vol% mixture of H<sub>2</sub>/CO<sub>2</sub>/N<sub>2</sub> with a total flow rate of 100 mL/min at different temperatures. The H<sub>2</sub>:CO<sub>2</sub> ratio was fixed at 4:1, which corresponds to the desired stoichiometry for CO<sub>2</sub> methanation (see Equation 1). CO<sub>2</sub> hydrogenation was studied at 5 isothermal stages at 200, 250, 300, 350 and 400 °C, each lasting for 1.5 h. The outlet gas is channelled through a drying tube filled with particles of silica gel desiccant for moisture removal. Then, the dried effluent gas was sent to gas analysers (ABB EL3020) for compositional analysis.

### 3. Results

#### 3.1. Catalyst characterisation

The synthesised fresh DFMs are comprehensively characterised to confirm the successful synthesis of the targeted formulae. First, the NiO loadings of the fresh DFMs were determined by thermogravimetric analysis (TGA), as shown in Fig. 3a. For all the fresh DFMs, 3 major weight losses are observed. The first drop at ~150 °C is attributed to the initiation of the reduction of NiO to Ni, accompanied by the decomposition of the organic residuals. The reduction of “bulk” NiO to Ni completes at ~200 °C, as shown and discussed in the TPR results below (Fig. 6). The second drop at ~350 °C is primarily associated with the decomposition of MgCO<sub>3</sub> to MgO. Therefore, the Ni active sites in DFM would have readily formed prior to the decomposition of MgCO<sub>3</sub> during the temperature-programmed hydrogenation experiments discussed in Section 3.2. The third drop at ~700 °C corresponds to the decomposition of CaCO<sub>3</sub> to CaO. The quantitative analysis of the second and third weight losses correspond well to the intended Ca:Mg ratios of the samples, as shown in Fig. 3b. The subsequent temperature-programmed oxidation (TPO) of the reduced DFMs (as shown in Fig. 3b) was then performed to measure the mass gain during the oxidation of Ni to NiO, which is used to estimate the mass fraction of NiO in the fresh DFMs. The TGA results tabulated in Table 1 show that, for all samples, the NiO mass fractions are close to 10 wt%, closely consistent with the targets of synthesis and the ICP results of these DFMs (Table S1).

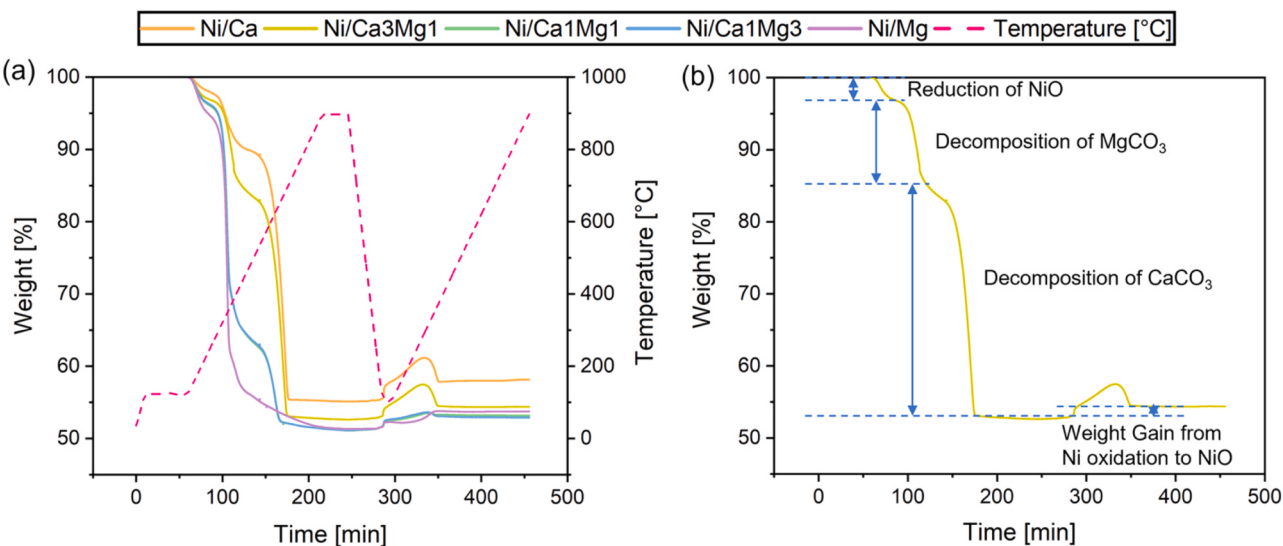


**Fig. 3.** (a) Weight loss - weight gain curves for all the fresh DFM samples undergoing TGA analysis including temperature programmed reduction followed by temperature programmed oxidation, (b) Interpretation of weight loss – weight gain curve for the Ni/Ca3Mg1 sample in TGA.

**Table 1**  
Summary of properties of Ni/carbonate DFM.

Sample	$S_{BET}$ [m <sup>2</sup> /g]	Ni particle size [nm]		Ni dispersion [%]	Metallic Ni surface area [m <sup>2</sup> /g]	NiO mass fraction [wt%]
		fresh	hydrogenated			
Ni/Ca	82	12 ± 6	13 ± 5	3.9	0.26	14.1
Ni/Ca3Mg1	115	-	-	5.9	0.39	8.3
Ni/Ca1Mg1	130	11 ± 4	13 ± 5	4.0	0.27	9.6
Ni/Ca1Mg3	127	-	-	2.3	0.14	8.3
Ni/Mg	178	19 ± 8	16 ± 9	0.8	0.05	11.3

Next, the porosity of the synthesised fresh DFM samples were characterised by BET analysis. **Table 1** shows the BET surface areas of the fresh DFM samples. It can be seen that the BET surface area decreased with increasing CaCO<sub>3</sub> content. This trend is consistent with the pure carbonate sorbents without Ni loading, because mesoporous MgCO<sub>3</sub> is expected to exhibit a higher area than amorphous CaCO<sub>3</sub> [66]. Comparing the Ni-loaded samples with the Ni-free carbonates (**Table S2**), it is observed that the deposition of Ni results in significant reduction in surface area. Looking at the change of the pore volumes and peak pore sizes (**Table S2**) before and after Ni loading, it can be seen that MgCO<sub>3</sub> and NiO/MgCO<sub>3</sub> have similar total pore volume (0.50 cm<sup>3</sup>/g and 0.46 cm<sup>3</sup>/g for MgCO<sub>3</sub> and Ni/MgCO<sub>3</sub>, respectively), while the pore size of MgCO<sub>3</sub> was approximately 3 times smaller than that of Ni/MgCO<sub>3</sub> (2.9 nm and 7.3 nm for MgCO<sub>3</sub> and Ni/MgCO<sub>3</sub>, respectively). Therefore, the loss in surface area upon NiO loading could be attributed to structural change and the loss of the small pores (e.g. due to sintering and pore blockage). [65] The morphology of the fresh and hydrogenated Ni/Ca, Ni/Ca1Mg1 and Ni/Mg are also examined by transition electron microscopy (TEM), as shown in **Fig. 4**. In all cases, Ni nanoparticles of similar size appear uniformly dispersed on the carbonates before and after hydrogenation. During the reduction of Ni/Mg, apparent morphological changes are observed as the original cube-shaped of MgCO<sub>3</sub> particles (**Fig. 4c**) thermally decomposed to form irregular agglomerates of MgO, as shown in **Fig. 4d**. Nevertheless, the sizes of the Ni particles remain largely unchanged (around 10–20 nm) after hydrogenation, as listed in **Table 1**. No serious Ni sintering was observed (**Fig. 4b, d and f**). Looking at the EDS elemental maps of Ni, Ca and Mg elements of the Ni/Ca1Mg1 DFM (**Fig. 4g, h and i**), it is observed that the reduced Ni particles are well dispersed on both two types of carbonates without any specific preference.

The XRD patterns of the fresh and hydrogenated Ni/Ca and Ni/Mg

DFMs (i.e., NiO/CaCO<sub>3</sub> and NiO/MgCO<sub>3</sub>, respectively) are shown in **Fig. 5a** and b, which shows no obvious diffraction peak, suggesting the amorphous nature of the NiO-impregnated precursors. [66] After 2 h reduction in 10 vol% H<sub>2</sub> at 400 °C (**Fig. 5a**), the amorphous CaCO<sub>3</sub> was transformed into the stable calcite phase, where the peaks at  $2\theta = 23.1^\circ$ ,  $29.4^\circ$ ,  $36.0^\circ$ ,  $39.5^\circ$ ,  $43.3^\circ$ ,  $47.5^\circ$ , and  $48.6^\circ$  corresponds to the calcite (012), (104), (110), (113), (202), (018) and (116) reflections, respectively [ICSD-18166]. The minor diffraction peaks at  $2\theta = 32.1^\circ$  and  $53.8^\circ$ , are indexed as the (111) and (220) reflections of CaO [ICSD-14922], respectively, suggesting that a small fraction of CaCO<sub>3</sub> was converted to CaO during reduction. At the same time, the diffraction peak at  $2\theta = 44.8^\circ$  and  $51.8^\circ$ , i.e., Ni (111) and (200) [ICSD-52265], indicate the formation of Ni metal upon the reduction of the NiO precursor. In comparison, the hydrogenation of Ni/Mg DFM resulted in the complete transformation of MgCO<sub>3</sub> to MgO, which showed characteristic peaks at  $2\theta = 37.2^\circ$ ,  $42.8^\circ$ ,  $62.0^\circ$  [ICSD-9863], while NiO was transformed to metallic Ni. The observed trend in phase transformation agrees with the common understanding that MgCO<sub>3</sub> is thermodynamically unstable and decomposes at 400 °C, while CaCO<sub>3</sub> remain relatively stable. [69,70] The surface compositions of the fresh and hydrogenated DFM samples are examined by X-ray photoelectron spectroscopy (XPS), as shown in **Fig. 5c** and d. The Ni 2p<sub>3/2</sub> spectra of the fresh and hydrogenated Ni/Ca DFM reflect the change in the chemical state of Ni, as shown in **Fig. 5c**. For fresh Ni/Ca DFM, the spectrum consists of a multiplet at 851.4 eV and 854.0 eV, both corresponding to NiO, and a satellite peak at 858.8 eV. For the hydrogenated Ni/CaCO<sub>3</sub>, the Ni 2p<sub>3/2</sub> binding energy changes to 854.2 eV with a satellite peak at 859.8 eV, which is attributed to the reduction of NiO and the formation of metallic Ni. [72, 73] Similarly, for Ni/MgCO<sub>3</sub>, the reduction of NiO to metallic Ni is observed after the hydrogenation of the fresh Ni/Mg DFM, where a multiplet at 851.4 eV and 854.6 eV (corresponding to NiO) with its

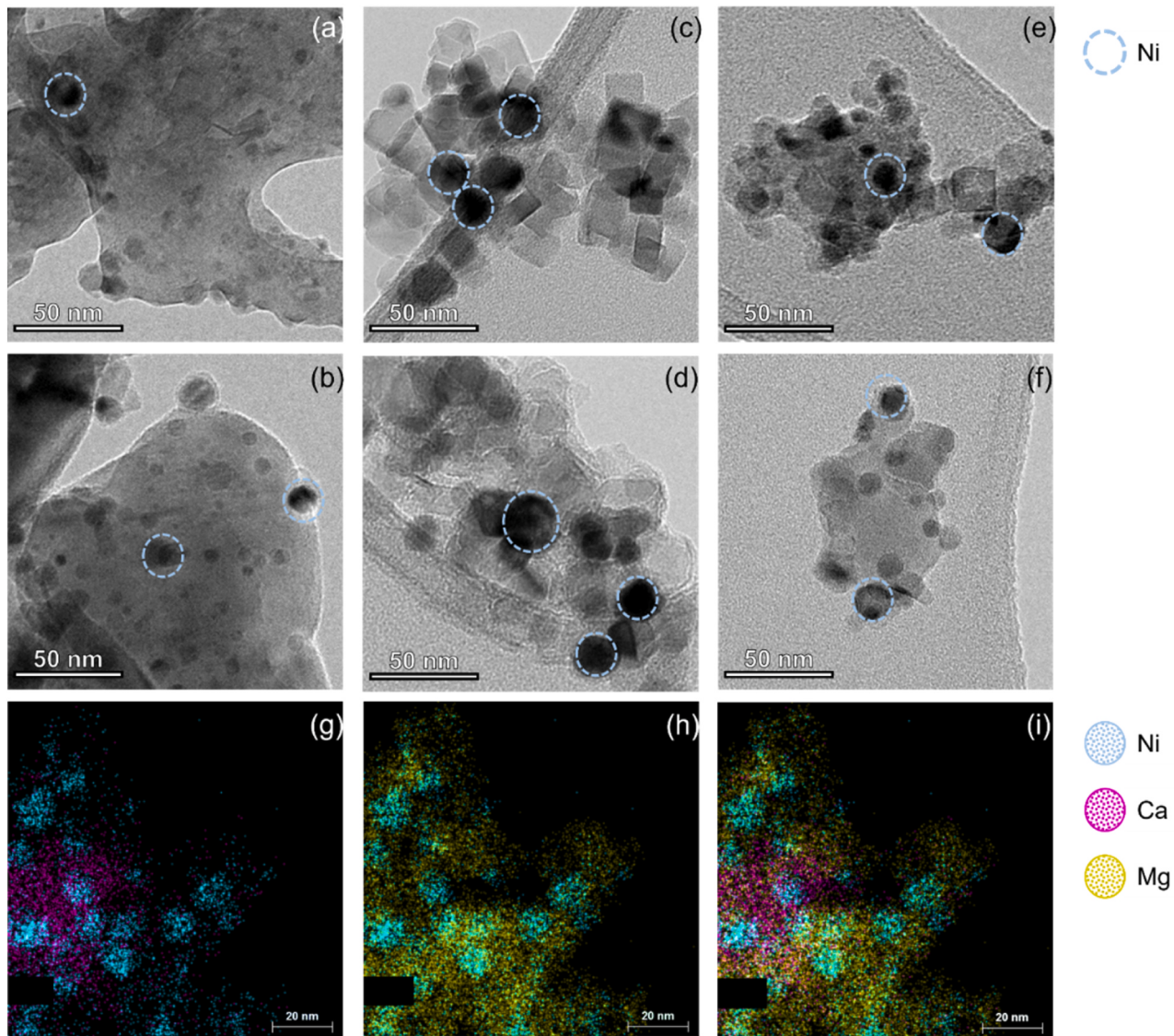


**Fig. 4.** TEM images of fresh and hydrogenated (a), (b) Ni/Ca; (c), (d) Ni/Mg; and (e), (f) Ni/Ca1Mg1; and EDS mapping images of (g) Ni-Ca, (h) Ni-Mg (i) Ni-Ca-Mg on hydrogenated Ni/Ca1Mg1.

satellite peak at 860.6 eV are presented. After the hydrogenation, the Ni 2p<sub>3/2</sub> signal appears at 854.1 eV, suggesting the formation of metallic Ni on the surface of the hydrogenated Ni/MgCO<sub>3</sub> (Fig. 5d).

The extent of interaction between Ni and the carbonate or oxide supports are characterised by H<sub>2</sub>-TPR of the fresh Ni/carbonate DFMs; the results are shown in Fig. 6a. Specifically, a TPR peak at higher temperatures suggests stronger metal-support interaction than a TPR peaks at a lower temperature. Accordingly, the TPR peaks can be categorised into 3 types according to the temperatures at which they occur: (i) 90–130 °C, which are assigned to the reduction of NiO not interacting with the support, e.g. bulk NiO, (ii) 150–200 °C, which are assigned to the reduction of NiO weakly interacting with the support, e.g. NiO at the NiO/carbonate interfaces, and (iii) > 800 °C, which are assigned to the reduction of NiO strongly interacting with the support, e.g. the formation of Ni-containing mixed oxide phases or solid solutions. For Ni/Mg, NiO strongly interacts with the support, exhibiting a large type (iii) TPR peak, with a small low-temperature peak corresponding to the formation of Ni metal, probably prior to the decomposition of MgCO<sub>3</sub>. The strong interaction between NiO and MgO support could originate from the formation of a solid solution between the two halite-structured oxide phases (i.e. decomposed from MgCO<sub>3</sub>), because the Ni<sup>2+</sup> in a MgO-rich

solid solution is much more difficult to reduce than unsupported NiO. [74] With increasing CaCO<sub>3</sub> contents (i.e., Ni/Ca1Mg3 and Ni/Ca1Mg1), the type (ii) peak gradually intensifies, likely owing to the introduction of weak interaction between NiO and CaCO<sub>3</sub>. When CaCO<sub>3</sub> contents become dominate (e.g., Ni/Ca3Mg1 and Ni/Ca), the type (iii) TPR peak almost vanishes; instead, type (i) and (ii) peaks become significant. For Ni/CaCO<sub>3</sub>, the absence of any type (iii) peak further signify that the type (iii) interaction is exclusively associated with a Ni/MgO interface. [75] In conclusion, the metal-support interaction is strong across the Ni/MgO interface, but weak across the Ni/CaO or Ni/CaCO<sub>3</sub> interface. [76].

The surface Ni dispersion on the hydrogenated DFMs was quantitatively determined using the results of CO pulse chemisorption, as shown in Table 1. A stoichiometric factor of CO to Ni atom of 1:1 is assumed. From Table 1, it can be seen that hydrogenated Ni/CaCO<sub>3</sub> has a Ni dispersion of 3.9%, which increases to 5.9% upon the addition of Mg (i.e., Ni/Ca3Mg1). Subsequent increase in Mg content (i.e., Ni/Ca1Mg1, Ni/Ca1Mg3 and Ni/Mg) resulted in the progressive decrease in Ni dispersion. In the extreme scenario of Ni/Mg (i.e. Ni/MgO), the Ni dispersion is only 0.8%, which can be attributed to the formation of NiO-MgO solid solution, which suppress the formation of metallic Ni during

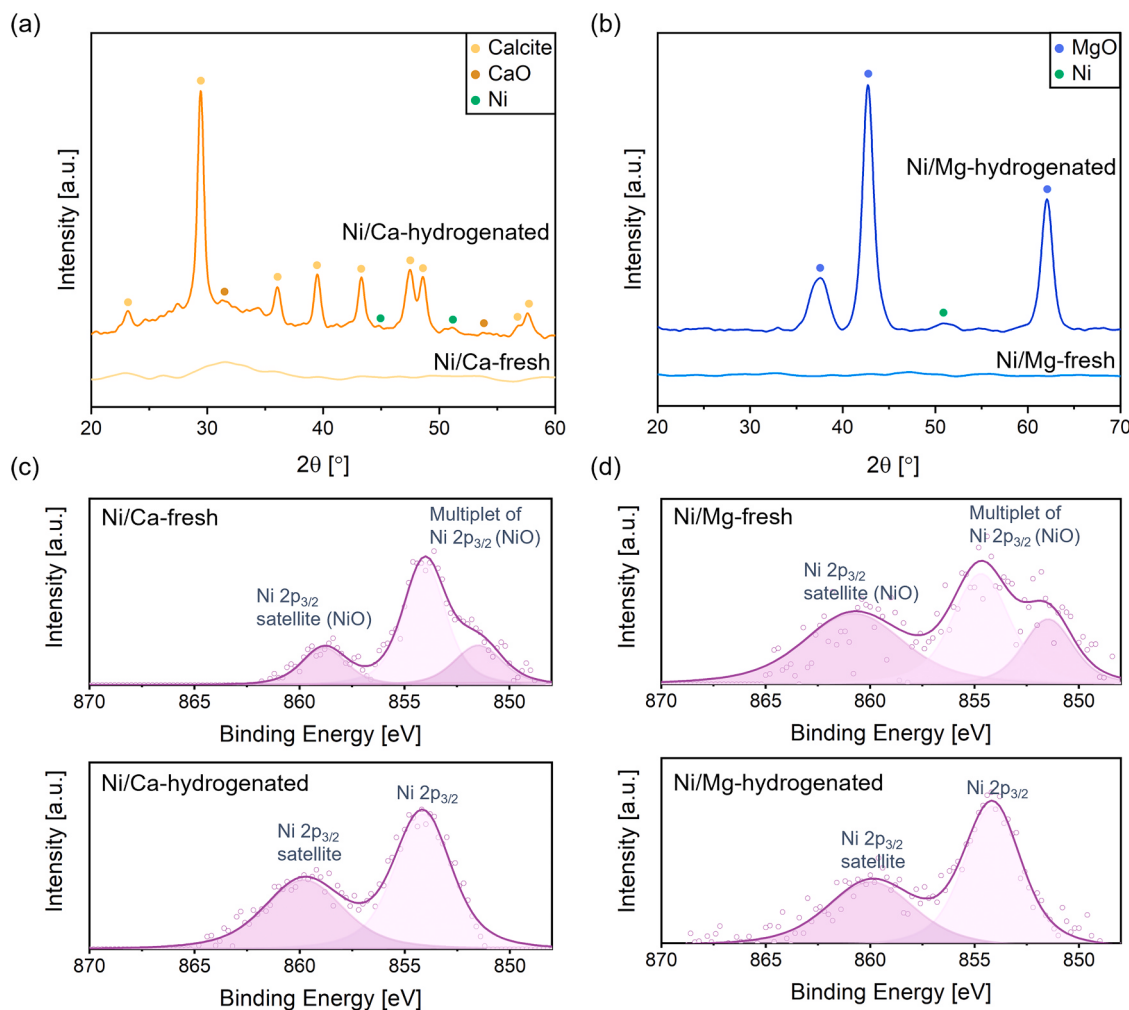


**Fig. 5.** XRD patterns of fresh and hydrogenated DFM of Ni/CA (a) and Ni/Mg (b); XPS Ni 2p<sub>3/2</sub> spectra of over fresh and hydrogenated DFM of Ni/CA (c) and Ni/Mg (d).

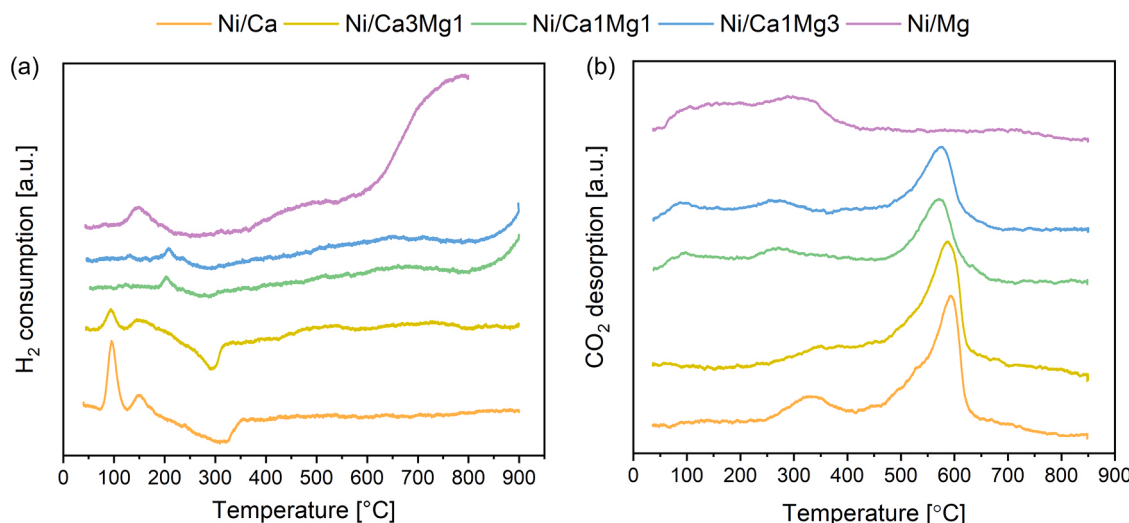


**Fig. 6.** (a) H<sub>2</sub>-TPR and (b) CO<sub>2</sub>-TPD results of the various Ni/carbonate DFM.

reduction (i.e. during hydrogenation), [75] while the metallic Ni precipitated from the solid solution are expect to interact strongly with the MgO support.

Surface alkalinity and basicity is also an important property for both

CO<sub>2</sub> sorbents, CO<sub>2</sub> hydrogenation catalysts, [18] and DFM. Here, CO<sub>2</sub>-TPD is used to characterise the stability of the carbonates, which in turn reflects the surface basicity of the DFM. In general, TPD peaks at higher temperatures correspond to high basicity and more stable

carbonates. As shown by the CO<sub>2</sub>-TPD results in Fig. 6b, two broad peaks at ~100 °C and ~275 °C can be seen in the TPD profiles of the Mg-rich samples, signifying the weak basic sites of MgO. A sharp peak at ~570–590 °C was seen in all Ca-containing samples, representing the strong basic sites on CaO. Therefore, the surface basicity of these Ni/carbonate samples, as characterised by CO<sub>2</sub>-TPD, reflects the alkalinities of the DFMs, i.e., Ca-rich DFMs has higher basicity than Mg-rich DFMs. According to the literature, moderate basicity, which corresponds to the TPD peaks at intermediate desorption temperatures would be ideal for catalytic CO<sub>2</sub> hydrogenation at moderate temperatures (~300–500 °C). [77] Tuning the surface basicity to suitable strength could promote interaction between the carbonates with the active metal sites, which enhances the CO<sub>2</sub> adsorption and hydrogenation to CH<sub>4</sub>. [18,41,78] These moderate basic sites could be seen in the two Ca-rich samples (i.e., Ni/Ca and Ni/Ca3Mg1). During ICCU cycles, the surface basicity of the various DFMs could play important roles in determining the rate and selectivity of the hydrogenation of the captured CO<sub>2</sub>. [79].

### 3.2. Direct hydrogenation of Ni/carbonates

Fig. 7a and b show the typical gas concentration profiles of CO, CH<sub>4</sub> and CO<sub>2</sub>, when Ni/Ca1Mg3 and Ni/Ca, respectively, were heated up from room temperature to 400 °C in flowing hydrogen. Here, the temperature programmed hydrogenation (TPH) results of Ni/Ca1Mg3 and Ni/Ca are chosen as examples for discussing the typical product profiles observed during the experiments. The full set of TPH results of all the samples studied, viz. Ni/Mg, Ni/Ca1Mg3, Ni/Ca1Mg1, Ni/Ca3Mg1 and Ni/Ca are shown in the Supporting Information (Fig. S2). For Ni/Ca1Mg3 (Fig. 7a), as the sample was heated up in H<sub>2</sub>, NiO is firstly reduced to metallic Ni below 200 °C to form the active sites for CO<sub>2</sub> and, or

carbonate hydrogenation. Then, a peak of CO<sub>2</sub> emerged, signifying carbonation decomposition, followed by a peak of CO and finally CH<sub>4</sub>. The sequence at which the gaseous products appeared suggests that the corresponding reactions producing them might be mechanistically sequential, i.e., CO might be produced from the gaseous CO<sub>2</sub> product, while CH<sub>4</sub> might be produced from the CO intermediate. For Ni/Ca, however, very little CO<sub>2</sub> or CO gas was released. Instead, CH<sub>4</sub> was directly formed during the hydrogenation of Ni/Ca. Fig. 7c shows the total amount of 3 C-containing gases produced (i.e., CO, CH<sub>4</sub> and CO<sub>2</sub>) during the temperature-programmed hydrogenation experiments. In general, the total amount of these 3 gases produced decreases with increasing Ca:Mg ratio. Ni/Mg produced the most C-containing gases, albeit primarily in the form of CO<sub>2</sub> (0.73 mmol) with trace amount of CO (0.02 mmol), whereas Ni/Ca produced the least amount, and mostly all in the form of CH<sub>4</sub> (0.12 mmol, while the amount of CO or CO<sub>2</sub> production was negligible). For Ni supported on mixtures of MgCO<sub>3</sub> and CaCO<sub>3</sub>, the amount of each gas produced and the corresponding product selectivity are in between the extremes of Ni/Mg and Ni/Ca. The trend in the total amount of CO, CH<sub>4</sub> and CO<sub>2</sub> gases produced can be explained by the fact that MgCO<sub>3</sub> would fully decompose during the temperature programme, releasing gaseous CO<sub>2</sub>. Ni/Mg produced little CO or CH<sub>4</sub> because little Ni sites were available from the incomplete reduction of the NiO-MgO solid solution. CO was only produced in samples containing MgCO<sub>3</sub>, suggesting that the CO originated from the hydrogenation of gas phase CO<sub>2</sub>, which re-adsorbed onto the catalyst sites and underwent RWGS. In contrast, the Ni/CaCO<sub>3</sub> interface yielded no gaseous CO<sub>2</sub>, since CaCO<sub>3</sub> is largely stable at 400 °C. Nevertheless, a substantial amount of CH<sub>4</sub> (with nearly 100% selectivity) was produced from the hydrogenation of Ni/CaCO<sub>3</sub>, suggesting that the CH<sub>4</sub> was produced via the direct hydrogenation of CaCO<sub>3</sub>.

The temperatures at which the rate of production of the 3 gases reach

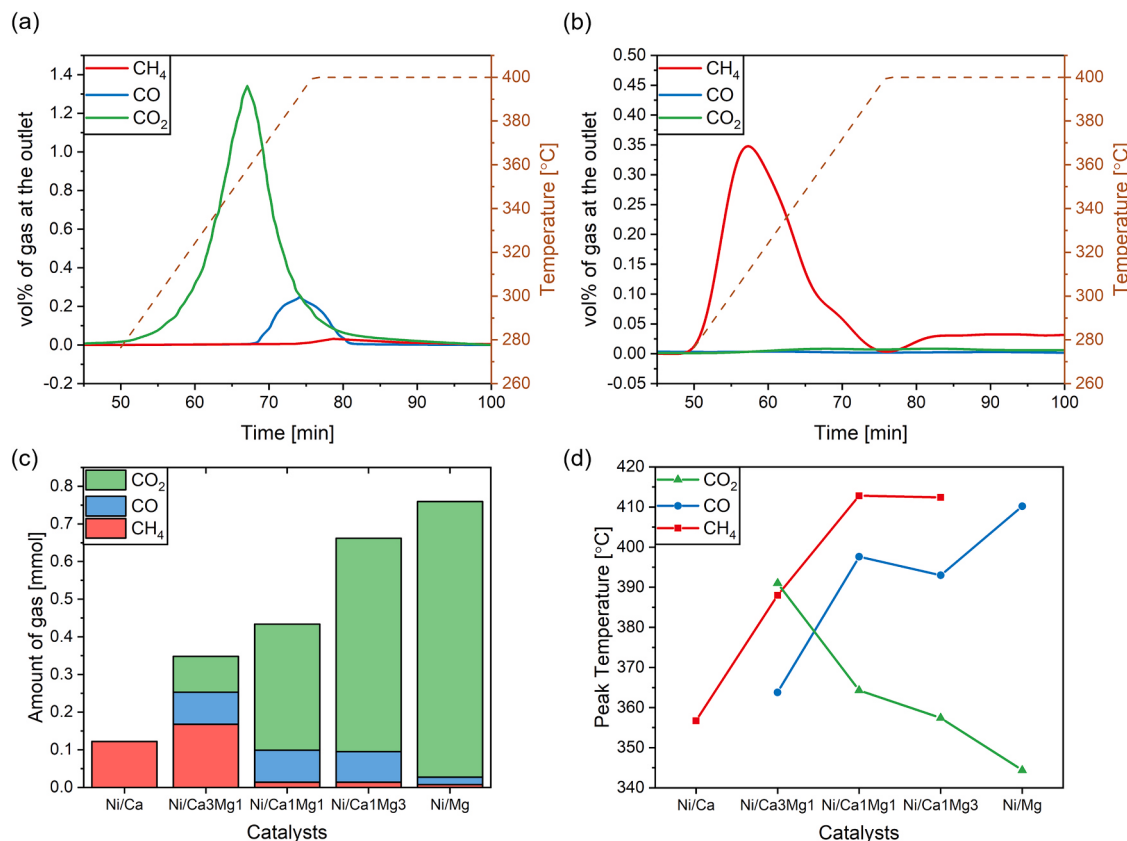


**Fig. 7.** Gas concentration profiles of CH<sub>4</sub>, CO<sub>2</sub> and CO on Ni/Ca1Mg3 (a) and Ni/Ca (b) during direct hydrogenation from 50° to 400°C, following by isothermal hydrogenation at 400 °C, both in 10% H<sub>2</sub>/N<sub>2</sub> at 1 atm; (c) amount of CH<sub>4</sub>, CO and CO<sub>2</sub> formation during direct hydrogenation experiments; (d) peak temperatures of CH<sub>4</sub>, CO and CO<sub>2</sub> formation during direct hydrogenation on Ni/carbonate DFMs.

maximum are deemed a characterisation of the reaction kinetics and plotted in Fig. 7d. As shown in Fig. 7d, as the Ca:Mg ratio increases, the temperature at which the rate of release of CO<sub>2</sub> maximises increases, because less and less MgCO<sub>3</sub> is available for thermal decomposition. For

example, the temperature at which the rate of release of CO<sub>2</sub> maximises was 344 °C for Ni/Mg sample, but when the Ca:Mg ratio was increased to 3:1, the corresponding peak temperature rose to 391 °C. Interestingly, the peak temperatures of both CO production and CH<sub>4</sub> production

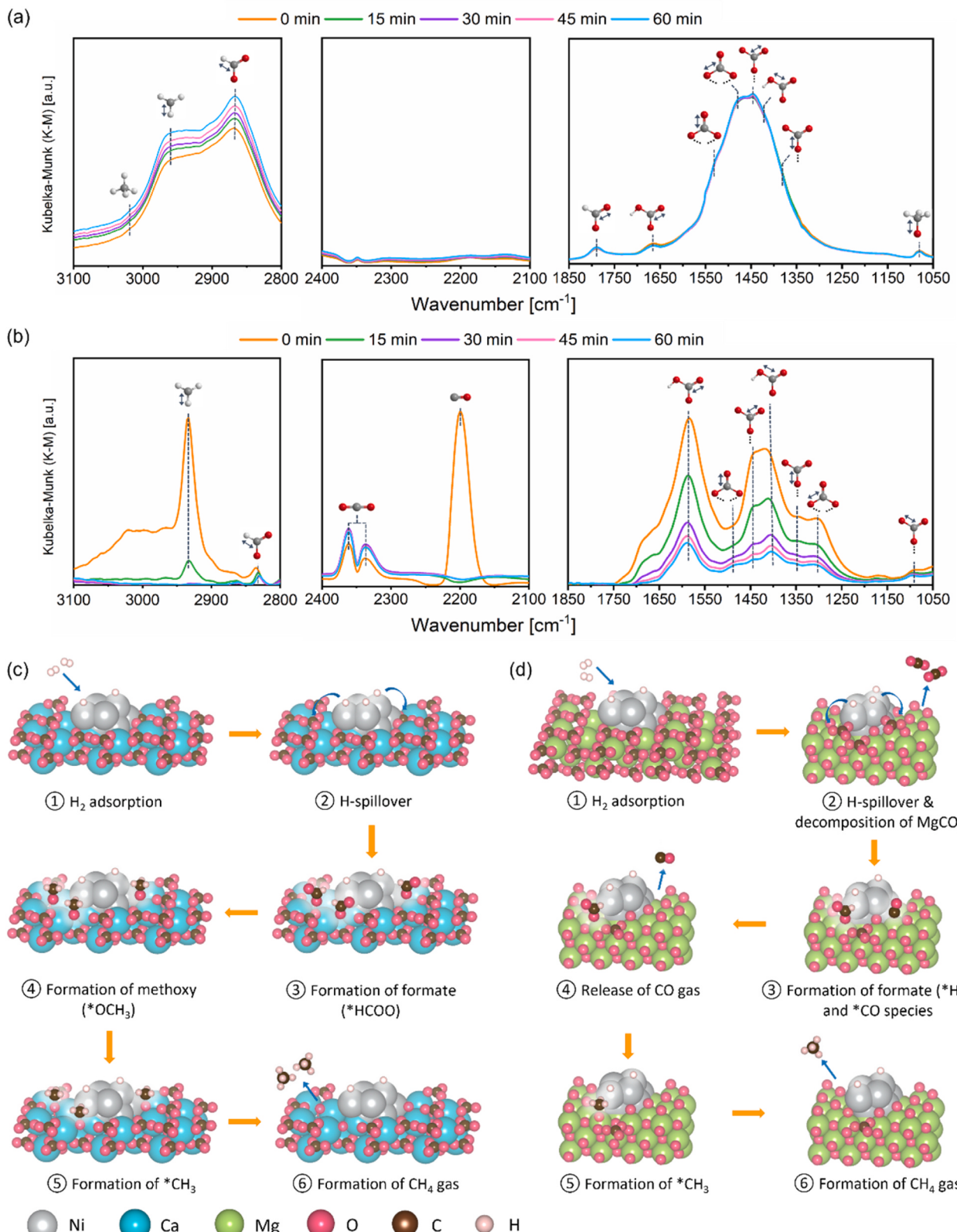


**Fig. 8.** Time-resolved in situ DRIFTS spectra of the direct hydrogenation of (a) Ni/Ca and (b) Ni/Mg in 25% H<sub>2</sub>/Ar at 1 atm total pressure and 400 °C over 1 h. (c) and (d) schematically illustrate the proposed reaction mechanism of direct hydrogenation on Ni/Ca and Ni/Mg, respectively.

decrease with increasing Ca:Mg ratio, especially the peak temperature of CH<sub>4</sub> production greatly dropped from 412 °C for Ni/Ca1Mg3 to 357 °C for Ni/Ca sample. This means high CaCO<sub>3</sub> content corresponds to enhanced rate of hydrogenation, suggesting that the presence of CaCO<sub>3</sub> kinetically favours the hydrogenation of carbonates or the surface-adsorbed CO<sub>2</sub>.

As discussed above and shown in Fig. 7, the temperature-programmed hydrogenation experiments suggest that the reaction pathways on Ni/MgCO<sub>3</sub> and Ni/CaCO<sub>3</sub> may be fundamentally different. The mechanistic origin of this difference is explored by in situ DRIFTS. Fig. 8a and b show the DRIFT spectra during the isothermal hydrogenation of Ni/CaCO<sub>3</sub> and Ni/MgCO<sub>3</sub> interfaces, respectively, at 400 °C. For Ni/CaCO<sub>3</sub> (Fig. 8a), IR signals corresponding to 3 different surface carbonate species can be seen: monodentate carbonates (1443 and 1385 cm<sup>-1</sup>), bidentate carbonates (1539, 1497, 1298 and 1275 cm<sup>-1</sup>), and bicarbonates (1660 and 1427 cm<sup>-1</sup>). Upon hydrogenation, the intensities of these carbonate peaks were progressively weakened over time, indicating their consumption. Concomitantly, the peaks corresponding to formate species emerge at 2850, 1788 and 1462 cm<sup>-1</sup>, implying the conversion of carbonates to surface formate groups by hydrogenation. [43,80–82] The gradual emergence of methoxy species (\*H<sub>3</sub>CO) peaks at 1080 cm<sup>-1</sup> as a possible product of formate hydrogenation, further suggests that the direct hydrogenation proceeds via the formate pathway on Ni/CaCO<sub>3</sub>, with the hydrogenation of methoxy being one of the rate-determining steps. The proposed formate pathway is schematically depicted in Fig. 8c. Firstly, H<sub>2</sub> gas is dissociated on Ni sites to generate \*H species, which spills over the interfacial CaCO<sub>3</sub> and reacts with the surface carbonates to form formate species. The formate species are successively hydrogenated by more \*H from the neighbouring Ni sites, to generate \*H<sub>3</sub>CO and eventually \*CH<sub>3</sub>, undergoing formate pathway for CO<sub>2</sub> methanation. Finally, upon hydrogenation of \*CH<sub>3</sub>, CH<sub>4</sub> is produced and desorbed. The hydrogenation of CO<sub>2</sub> adsorbed species or surface carbonates over Ni sites upon the addition of H<sub>2</sub>, with formate species as key intermediates, was reported on a Ni-Na<sub>2</sub>O/Al<sub>2</sub>O<sub>3</sub> DFM for CO<sub>2</sub> capture and in situ methanation as well. [62].

Unlike Ni/CaCO<sub>3</sub>, much weaker characteristic IR peaks of formate species are observed throughout the in situ DRIFTS experiment of Ni/MgCO<sub>3</sub>, as shown in Fig. 8b. In addition to the gradual weakening of the

signals associated with surface carbonates and gaseous CO<sub>2</sub> due to MgCO<sub>3</sub> decomposition (2362 and 2337 cm<sup>-1</sup>), a small formate peak, which also weakens over time, can be observed at 2832 cm<sup>-1</sup>. At the same time, an intense peak corresponding to a surface-adsorbed CO species (2202 cm<sup>-1</sup>) is also observed at *t* = 0 but quickly diminishes, [81] probably as a result of direct C=O cleavage of CO<sub>2</sub> or RWGS. [83, 84] Therefore, both the RWGS pathway and the formate pathway could be simultaneously present on Ni/MgCO<sub>3</sub>. Given the weak formate peak relative to the intense CO peak, it is probably that RWGS dominates the reaction on the Ni/MgCO<sub>3</sub> sample, as schematically illustrated in Fig. 8d. For hydrogenation on Ni/MgCO<sub>3</sub> at 400 °C, firstly, MgCO<sub>3</sub> would decompose to MgO and then CO<sub>2</sub> gas is released. The released CO<sub>2</sub> would react with the \*H species generated from H<sub>2</sub> dissociation on Ni sites to form either formate intermediate or get reduced to \*CO species by RWGS pathway. The formed \*CO species would be desorbed and produce CO gas, while the formate species are further hydrogenated to CH<sub>4</sub> gas by formate pathway.

The hydrogenation of Ni/Ca will directly transform CaCO<sub>3</sub> to CaO at a temperature where CaCO<sub>3</sub> is expected to be stable in conventional carbon capture cycles (e.g., 400 °C). To further investigate the hydrogenation behaviour and reaction model on Ni/CaCO<sub>3</sub>, the hydrogenation duration of Ni/CaCO<sub>3</sub> was prolonged to 24 h. The rate of CH<sub>4</sub> formation and in situ DRIFTS during the 24 h hydrogenation experiment are shown in Fig. 9a and b, respectively. From Fig. 9a, there is an initial peak in the rate of CH<sub>4</sub> formation, which dropped to a steady value after 1 h. Correspondingly, the DRIFTS time series shows an initial quick drop of carbonate peak intensity in the first 0.5 h of the experiment, after which the intensities of the carbonate peaks stabilised. The evidence observed suggests the presence of two reaction phases: (i) a kinetically fast phase corresponding to the hydrogenation of CaCO<sub>3</sub> near the Ni/CaCO<sub>3</sub> interface and, or surface carbonates, followed by (ii) a slow phase corresponding to the hydrogenation of bulk CaCO<sub>3</sub>, as depicted Fig. 9d. The proposed two-phase reaction model is supported by experimental evidence previously reported in the literature. [19] An analysis of the TEM image of a Ni/CaCO<sub>3</sub> sample after 1 h of hydrogenation (Fig. 9c) further corroborate the reaction model. From Fig. 9c, it can be seen that, after 1 h of hydrogenation, a Ni particle is surrounded by CaO (with lattice fringes of 0.267 nm, assigned to CaO (111) plane) as a result of the direct hydrogenation of CaCO<sub>3</sub> during the fast stage. At > 5 nm away

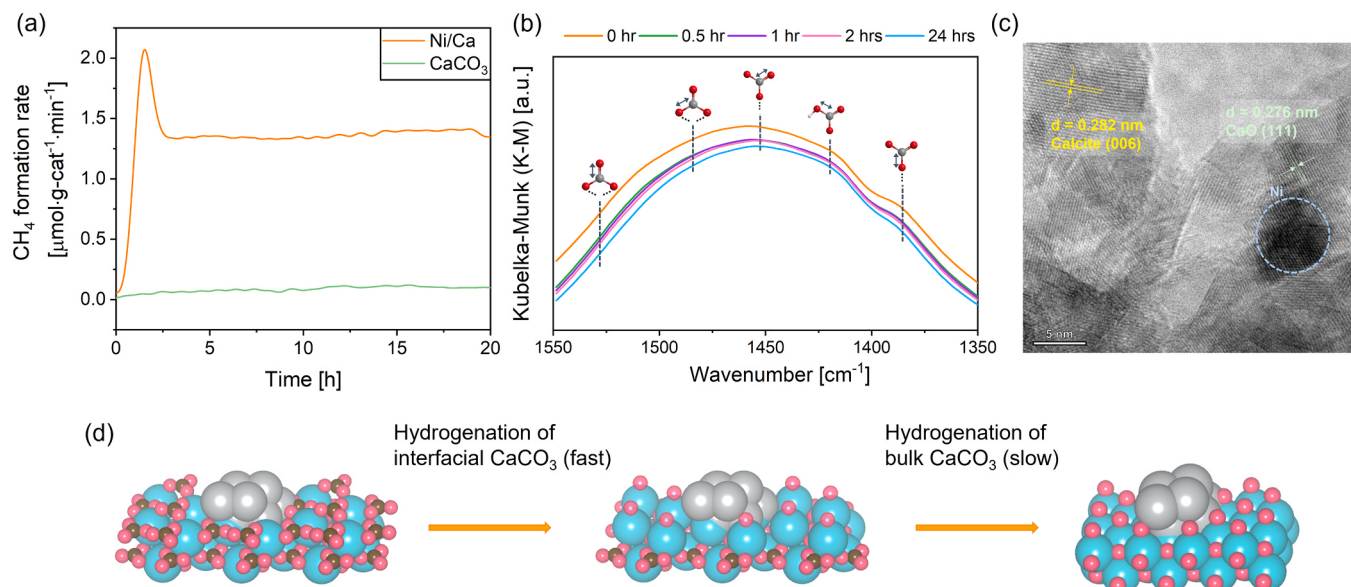


**Fig. 9.** (a) Gas profile of rate of CH<sub>4</sub> formation during the hydrogenation (in 10% H<sub>2</sub>/N<sub>2</sub> at 1 atm total pressure) of Ni/Ca and unloaded CaCO<sub>3</sub> at 400 °C over 20 h. (b) in situ DRIFTS spectra showing the evolution of surface carbonate species during the hydrogenation of Ni/Ca (in 10% H<sub>2</sub>/N<sub>2</sub> at 1 atm total pressure) at 400 °C over 24 h. (c) TEM image of a hydrogenated Ni/CaCO<sub>3</sub> sample; the blue circle indicates a Ni particle. (d) Schematic illustration of the progressive hydrogenation of Ni/CaCO<sub>3</sub> over time.

from the Ni particle,  $\text{CaCO}_3$  (with lattice fringes of 0.282 nm, corresponding to calcite (006) plane) remains present and yet to be hydrogenated by the slow stage. However, the exact nature of the reaction front and the associated mass transfer scheme for this slow phase, be it (i) hydrogen spill over, (ii) diffusion of carbonate species, (iii) transfer hydrogenation via the diffusion of hydrogenated intermediates or (iv) a combination of all of the above, is not clear and merits further investigation in future studies.

### 3.3. Integrated $\text{CO}_2$ capture and utilisation cycles

The evolution of the Ni/carbonate interfaces is investigated by subjecting the samples to 15 cycles of  $\text{CO}_2$  capture and hydrogenation, as shown in Fig. 10. Fig. 10a shows the gas concentration profiles of CO,  $\text{CH}_4$  and  $\text{CO}_2$  at the reactor outlet during the first, second, third, 13th, 14th and 15th ICCU cycles, when Ni/Ca was used as the DFM. In each cycle,  $\text{CH}_4$  is the dominating product during the hydrogenation stage, while trace amount of CO was generated during the  $\text{CO}_2$  capture stage. The latter can be possibly explained by (1) the oxidation of surface Ni atoms by  $\text{CO}_2$ , [17] or (2) the RWGS reaction between the incoming  $\text{CO}_2$  gas and chemisorbed  $\text{H}_2$  on the Ni surface, formed during the previous hydrogenation step. [60] The total amount of gaseous product formed in each cycle, over 15 ICCU cycles is shown in Fig. 10b. In general, more  $\text{CH}_4$  is formed on samples that are richer in  $\text{CaCO}_3$ , in line with the trend shown in Fig. 6. In the 15th cycle, the amount of  $\text{CH}_4$  formed on Ni/Ca (1.28 mmol/g) is 23.5 times of that on Ni/Mg (0.054 mmol/g), showing a significant disparity in their methanation activity. Moreover, Ni/Ca sample could produce a relatively consistent amount of  $\text{CH}_4$  per cycle, from the 3rd cycle onwards, whereas the other DFMs show significant decay in their ability to produce  $\text{CH}_4$ . In addition to sintering, which would result in the reduction in surface area available for  $\text{CO}_2$  conversion and destruction of pore structure that are essential to efficient mass transfer, the rapidly deterioration of the Mg-containing DFMs may also be attributed to the gradual and irreversible consumption of carbonates (both  $\text{MgCO}_3$  and  $\text{CaCO}_3$ ) over consecutive cycles without effective

regeneration. In contrast, the cyclic CO yield is consistent throughout the 15 cycles, regardless of the composition of the DFMs.

As shown in Fig. 9, both surface and bulk  $\text{CaCO}_3$  can be hydrogenated to produce  $\text{CH}_4$ . To examine whether all the  $\text{CH}_4$  produced by Ni/Ca is a result of hydrogenation of regenerable carbonates (instead of a cumulative and irreversible consumption of pre-formed  $\text{CaCO}_3$  in the sample), we repeated the ICCU cycling experiment using a pre-calcined Ni/Ca (i.e. Ni/CaO) as the starting material. The pre-calcination was done by subjecting Ni/ $\text{CaCO}_3$  in 100 mL/min  $\text{N}_2$  at 850 °C for 1 h to fully decompose the  $\text{CaCO}_3$  support to CaO. The corresponding results, as shown in Fig. 10c, indicate that the pre-calcined Ni/Ca (i.e., Ni/CaO) shows a similar cyclic performance of  $\text{CH}_4$  production over 15 ICCU cycles, with the exception of the first cycle, in which no carbonate was available in Ni/CaO to hydrogenation. Similar amount of  $\text{CH}_4$  was produced by Ni/CaO in each cycle (e.g., ~1.26 mmol/g at the 7th cycle, as shown in Fig. 10c) as the experiment starting with Ni/ $\text{CaCO}_3$ . In addition, as shown in Fig. S3, the profiles of rate of production of  $\text{CH}_4$  by the hydrogenation of a Ni/CaO DFM are similar to those of a Ni/ $\text{CaCO}_3$  DFM (Fig. 10a), depicting the both fast hydrogenation of the surface carbonate and the slow hydrogenation of the bulk carbonate. Therefore, the results of this control experiment confirm that both the surface and the bulk  $\text{CaCO}_3$  that is consumed (hydrogenated) from Ni/Ca in each ICCU cycle can be regenerated in the subsequent cycle. Furthermore, by comparing the total amount of  $\text{CH}_4$  formation during the hydrogenation step with the amount of  $\text{CO}_2$  available in the surface monolayer of Ni/ $\text{CaCO}_3$  (Table S3) it is clear that both  $\text{CO}_2$  capture and carbonate hydrogenation of Ni/ $\text{CaCO}_3$  involves reactions beyond the surface monolayer. Accordingly, approximately 10.5% of all the carbonate available in Ni/ $\text{CaCO}_3$  participates in the ICCU cycles, under the given operating conditions.

Fig. 11a and b show the diffraction patterns of the Ni/Ca and Ni/Mg samples after 15 ICCU cycles. Similar to the hydrogenated samples shown in Fig. 9c, which represent hydrogenated DFMs experiencing the first cycle, metallic Ni, calcite and CaO are both present in the cycled Ni/Ca in its hydrogenated state. For Ni/MgO, only MgO can be observed. No

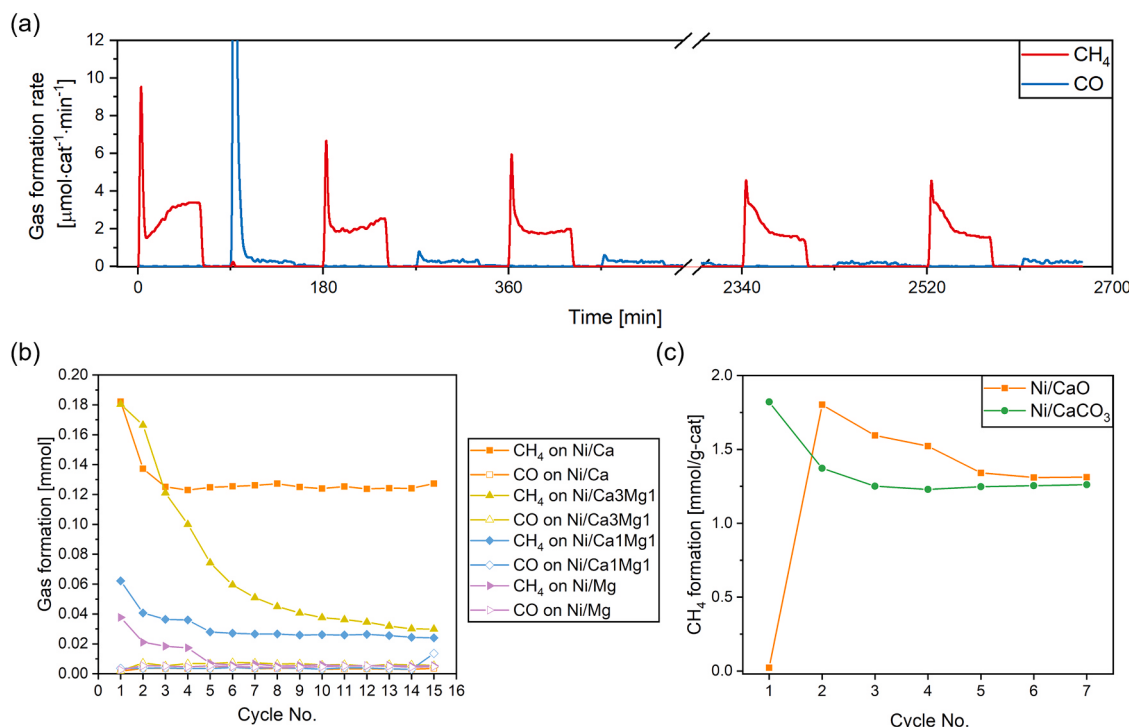


**Fig. 10.** (a)  $\text{CH}_4$  and CO profiles during two-step  $\text{CO}_2$  capture and hydrogenation on Ni/Ca over 15-cycles at 400 °C; (b) Results of two-step  $\text{CO}_2$  capture and hydrogenation over 15-cycles at 400 °C: amount of  $\text{CH}_4$  and CO formed during the hydrogenation and capture stages, respectively, in each cycle; (c) Amount of  $\text{CH}_4$  formation on Ni/Ca starting from Ni/CaO and Ni/ $\text{CaCO}_3$  over 7 ICCU cycles.

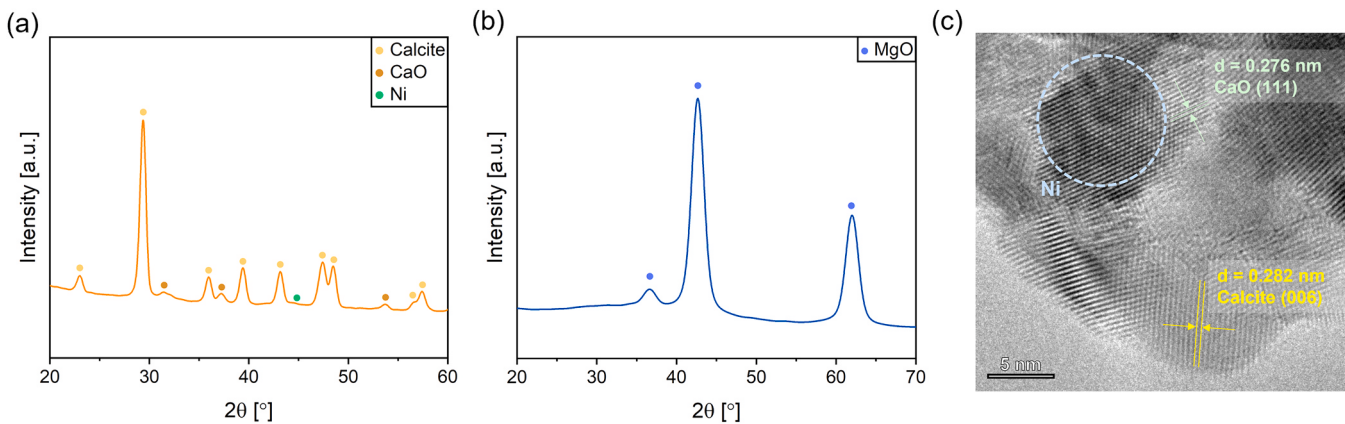


**Fig. 11.** XRD patterns of cycled catalysts of Ni/Ca (a) and Ni/Mg (b) after 15 ICCU cycles; (c) TEM image with lattice fringes of cycled Ni/Ca catalysts after 15 cycles of CO<sub>2</sub> capture-hydrogenation.

diffraction peak of Ni could be observed in the XRD of the cycled samples, probably because of the small sizes of Ni particles, as well as the formation of NiO-MgO solid solution mitigating the formation of Ni particles. The TEM image of cycled Ni/Ca, as shown Fig. 11c, reveals a structure that is highly similar to a freshly hydrogenated Ni/Ca (Fig. 9c), i.e., a nickel nanoparticle is surrounded by CaO, while CaCO<sub>3</sub> can be observed further away. In conclusion, in the case of Ni/Ca DFM, the reaction pathway, catalytic mechanism, catalyst structure and reaction model remain largely unchanged over ICCU cycles. Therefore, the findings in the present study should be relevant to understanding the

behaviour of DFMs over long term ICCU operations.

#### 4. Discussion

The hydrogenation of a carbonated catalyst surface is often used to examining the catalytic mechanism of conventional CO<sub>2</sub> hydrogenation reactions. Here, we examine the analogy between the performance of DFMs over ICCU cycles and that during conventional CO<sub>2</sub> hydrogenation. Fig. 12a and b show the CO<sub>2</sub> conversion and CH<sub>4</sub> selectivity when the five Ni/carbonate DFMs are used as conventional CO<sub>2</sub>

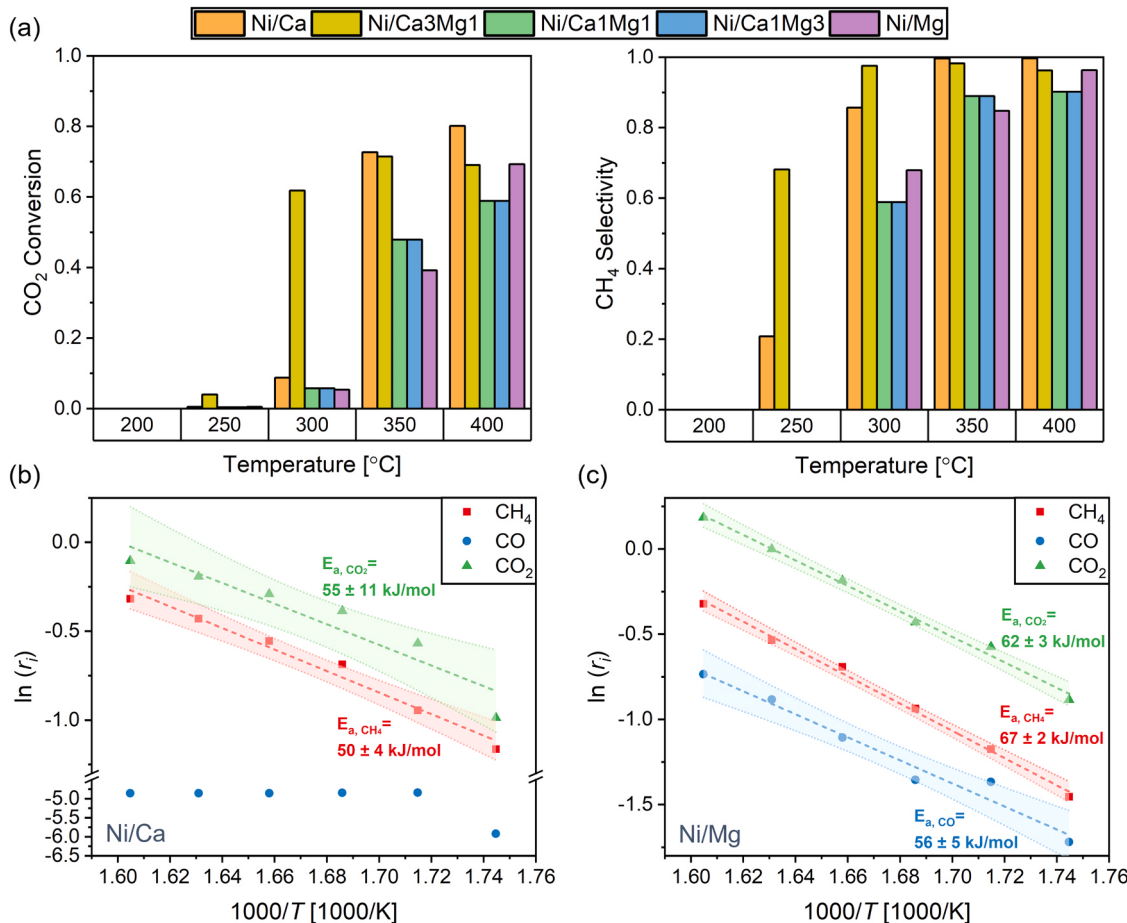


**Fig. 12.** (a) Conventional one-step CO<sub>2</sub> methanation performance test results on 8 wt% Ni loading samples (H<sub>2</sub>:CO<sub>2</sub> = 4:1); Arrhenius plots of CH<sub>4</sub> formation, CO formation and CO<sub>2</sub> consumption during catalytic CO<sub>2</sub> hydrogenation on (b) Ni/Ca and (c) Ni/Mg.

hydrogenation catalysts over the temperature range of 200–400 °C. For all 5 samples, the CO<sub>2</sub> conversion and CH<sub>4</sub> selectivity increased with increasing temperatures. Fig. 12a shows that, among all samples, Ni/Ca achieved the highest CH<sub>4</sub> yield of 80.0% with a CH<sub>4</sub> selectivity of near unity (>99%), corresponding to a specific CH<sub>4</sub> formation rate of 105.6 μmol·s<sup>-1</sup>·g<sup>-1</sup> at 400 °C. The two Ca-rich supports, Ni/Ca and Ni/Ca<sub>3</sub>Mg<sub>1</sub>, exhibited higher CO<sub>2</sub> conversion and higher CH<sub>4</sub> selectivity at moderate temperatures from 300° to 350°C than the other 3 Mg-rich samples. In fact, at any given temperature, samples richer in Ca tend to show higher CO<sub>2</sub> conversion and higher CH<sub>4</sub> selectivity. However, the difference in CO<sub>2</sub> conversion and CH<sub>4</sub> selectivity between different samples are far less profound during conventional CO<sub>2</sub> hydrogenation than during ICCU cycles, in which Ni/Mg shows significantly low CH<sub>4</sub> yield and CH<sub>4</sub> selectivity (96% CH<sub>4</sub> selectivity during conventional CO<sub>2</sub> hydrogenation, while 53% CH<sub>4</sub> selectivity on 15th ICCU cycle at 400 °C). Such disparity suggests that the sources of CO<sub>2</sub> may be fundamentally different during conventional CO<sub>2</sub> hydrogenation and ICCU cycles. For conventional hydrogenation, all CO<sub>2</sub> comes from the gas feed. During ICCU, the reaction on Ni/MgCO<sub>3</sub> relies on a continuous supply of CO<sub>2</sub> in the gas phase, whilst the reaction on Ni/CaCO<sub>3</sub> would proceed via the direct hydrogenation of readily available carbonates, both at the surface and in the bulk.

The differences in the catalytic performance of Ni/Ca and Ni/Mg during conventional CO<sub>2</sub> hydrogenation and ICCU suggests that the different metal-support interfaces (Ni/CaCO<sub>3</sub> vs Ni/MgCO<sub>3</sub>) and their subsequent interactions could lead to different CO<sub>2</sub> hydrogenation reaction pathways. In conventional CO<sub>2</sub> hydrogenation, 3 reaction pathways have been proposed: (1) direct C=O bond cleavage followed by possible CO hydrogenation, (2) RWGS followed by CO hydrogenation, and (3) the hydrogenation of formate (i.e., the formate pathway). [83, 85, 86] The first two pathways involve the formation of \*CO as a key intermediate, while the last involves the hydrogenation of CO<sub>2</sub> or carbonate to formate, which is further hydrogenated.

To probe the relationship between CO formation, CH<sub>4</sub> formation and CO<sub>2</sub> activation, the activation energies of CO formation ( $E_{a,CO}$ ), CH<sub>4</sub> formation ( $E_{a,CH_4}$ ) and CO<sub>2</sub> consumption ( $E_{a,CO_2}$ ) during conventional CO<sub>2</sub> hydrogenation on Ni/Ca and Ni/Mg were determined based on the specific rates measured at low CO<sub>2</sub> conversions (<20%). [87] The results are shown in Fig. 12b and c. For Ni/Mg,  $E_{a,CO}$  (56 ± 5 kJ/mol) <  $E_{a,CH_4}$  (67 ± 2 kJ/mol), meaning that the formation of CO is energetically favoured over the formation of CH<sub>4</sub>. At the same time,  $E_{a,CO}$  (56 ± 5 kJ/mol) <  $E_{a,CO_2}$  (62 ± 3 kJ/mol), suggesting that CO formation is possibly a prerequisite to CH<sub>4</sub> formation. For Ni/Ca, the amount of CO formation is too little to accurately estimate  $E_{a,CO}$ , while the activation energy of CH<sub>4</sub> is 50 ± 4 kJ/mol, similar to the activation energy of CO<sub>2</sub> of 55 ± 11 kJ/mol, suggesting that CO\* is an unlikely intermediate for CO<sub>2</sub> methanation. Therefore, CO<sub>2</sub> hydrogenation on Ni/Ca is most likely to proceed via the formate pathway. [83, 84].

To complement the analysis of apparent activation energies. The difference in reaction pathways on Ni/MgCO<sub>3</sub> and Ni/CaCO<sub>3</sub> are also examined by measuring the surface significant species during conventional CO<sub>2</sub> hydrogenation using in situ DRIFTS. On Ni/CaCO<sub>3</sub>, both formate and methoxy species are observed, together with peaks corresponding to gaseous CH<sub>4</sub> at 3015 cm<sup>-1</sup>, as shown in Fig. 13a. The observed peak can be explained by the formate pathway, in which the carbonate species is firstly hydrogenated to formate (\*HCOO), which is successively hydrogenated to form methoxy (\*H<sub>3</sub>CO), methyl \*CH<sub>3</sub> (showing a peak in 2966 cm<sup>-1</sup>) and eventually gaseous CH<sub>4</sub>. [83, 84] The reaction pathway is schematically illustrated in Fig. 13c, which is similar to the formate pathway proposed for Ni/CaCO<sub>3</sub> during ICCU cycles. On Ni/MgCO<sub>3</sub>, the same surface species could be observed, albeit with much lower intensities of formate species, indicating that the formate pathway is insignificant on Ni/MgCO<sub>3</sub> (Fig. 13b). Furthermore, the peaks corresponding to CO gas (2294 and 2143 cm<sup>-1</sup>) are observed, [83, 84] that direct CO<sub>2</sub> dissociation and/or RWGS pathway is prevailing on

Ni/MgCO<sub>3</sub>, as schematically depicted in Fig. 13d. [88].

The experimental results have provided conclusive evidence showing that CO<sub>2</sub> hydrogenation on Ni/CaCO<sub>3</sub> and Ni/MgCO<sub>3</sub> are likely to proceed via formate and CO intermediates, respectively. Specifically, the CO (RWGS) pathway is responsible for the high CO yield and the low CH<sub>4</sub> selectivity on Ni/MgCO<sub>3</sub> (53% CH<sub>4</sub> selectivity on 15th ICCU cycle at 400 °C), in agreement with the experimental observations during both conventional CO<sub>2</sub> hydrogenation and ICCU cycles. In contrast, the Ni/CaCO<sub>3</sub> interface facilitates the efficient hydrogenation of carbonate to formate, which could be further hydrogenated at the metal/carbonate interface, facilitated by hydrogen spill over. This enhanced formate pathway is likely to arise from the interactions between Ni and CaCO<sub>3</sub>, the moderate stability of CaCO<sub>3</sub>, as well as the moderately alkalinity of Ni/CaO.

Based on the discussion so far, it is conducive that an efficient formate pathway may be the key for achieving high CH<sub>4</sub> yield and high CH<sub>4</sub> selectivity during both ICCU and conventional CO<sub>2</sub> hydrogenation. In the present study, experimental investigations under both ICCU and conventional CO<sub>2</sub> hydrogenation conditions suggest that the reaction pathway and catalytic mechanism under the two operating regimes may be related: formate pathway is dominating during both the hydrogenation of a Ni/CaCO<sub>3</sub> interface during ICCU and the hydrogenation of adsorbed CO<sub>2</sub> during conventional catalytic CO<sub>2</sub> methanation on Ni/CaCO<sub>3</sub>. In comparison, Ni/MgCO<sub>3</sub> exhibits high selectivity towards the production of CO via the RWGS pathway, while methanation reaction via the formate pathway may also be feasible in the presence of a substantial CO<sub>2</sub> pressure (e.g. in the case of co-feeding gaseous CO<sub>2</sub> and H<sub>2</sub>). Admittedly, the surface coverage of CO<sub>2</sub> on the DFMs under the two operating regimes may be rather different, i.e., the DFM would have a lower CO<sub>2</sub> coverage during direct hydrogenation than during conventional CO<sub>2</sub> hydrogenation. However, the structure and chemical nature of the bifunctional metal/carbonate interface, may play a more dominant role in determining the reaction mechanism during CO<sub>2</sub> transformation than the partial pressure of CO<sub>2</sub> and surface coverage within the operating regime of interest. This means that the hydrogenation of CO<sub>2</sub> may proceed via similar reaction pathways with similar rate-determining steps (e.g., the hydrogenation of formate, etc) for the two reaction regimes. Indeed, it is experimentally observed that the apparent CH<sub>4</sub> product yield and selectivity measured under both ICCU cycles and conventional CO<sub>2</sub> hydrogenation conditions share a similar trend, i.e. higher CaCO<sub>3</sub> content corresponds to higher CH<sub>4</sub> selectivity, as illustrated by a correlation plot shown in Fig. 14. In other words, the two-step carbonation-hydrogenation cycles (ICCU cycles) could be employed as an insightful approach to study the catalytic conversion of CO<sub>2</sub> on DFMs as well as other hydrogenation catalysts. Lastly, it should be noted that, in foreseeable commercial applications, there may be an even greater disparity between the operating conditions of ICCU and those of conventional hydrogenation, e.g., the DFM would be exposed to considerable partial pressures of oxygen, moisture and other impurities during ICCU [16, 42]. Therefore, whether the observed correlation in reaction pathway and catalytic mechanism between the two regimes still hold should be experimentally verified in future studies.

## 5. Conclusion

The two-step CO<sub>2</sub> capture-hydrogenation process, using Ni-based DFMs, is studied on a model Ni/carbonate structures over moderate temperature ranges of 300–400 °C. The hydrogenation behaviour of Ni/CaCO<sub>3</sub> and Ni/MgCO<sub>3</sub> interfaces are found to be drastically different. Based on the in situ DRIFTS results, on Ni/CaCO<sub>3</sub>, the hydrogenation reaction proceeds via the direct hydrogenation to carbonate, via formate, methoxy and methyl intermediates, eventually forming CH<sub>4</sub>. On Ni/MgCO<sub>3</sub>, the reaction proceeds following the thermal decomposition of MgCO<sub>3</sub> to produce gaseous CO<sub>2</sub>, which subsequently adsorbs at the Ni/MgO interface to produce CO, which can be further hydrogenated to CH<sub>4</sub> with low CH<sub>4</sub> selectivity. Over 15 ICCU cycles at 400 °C, the

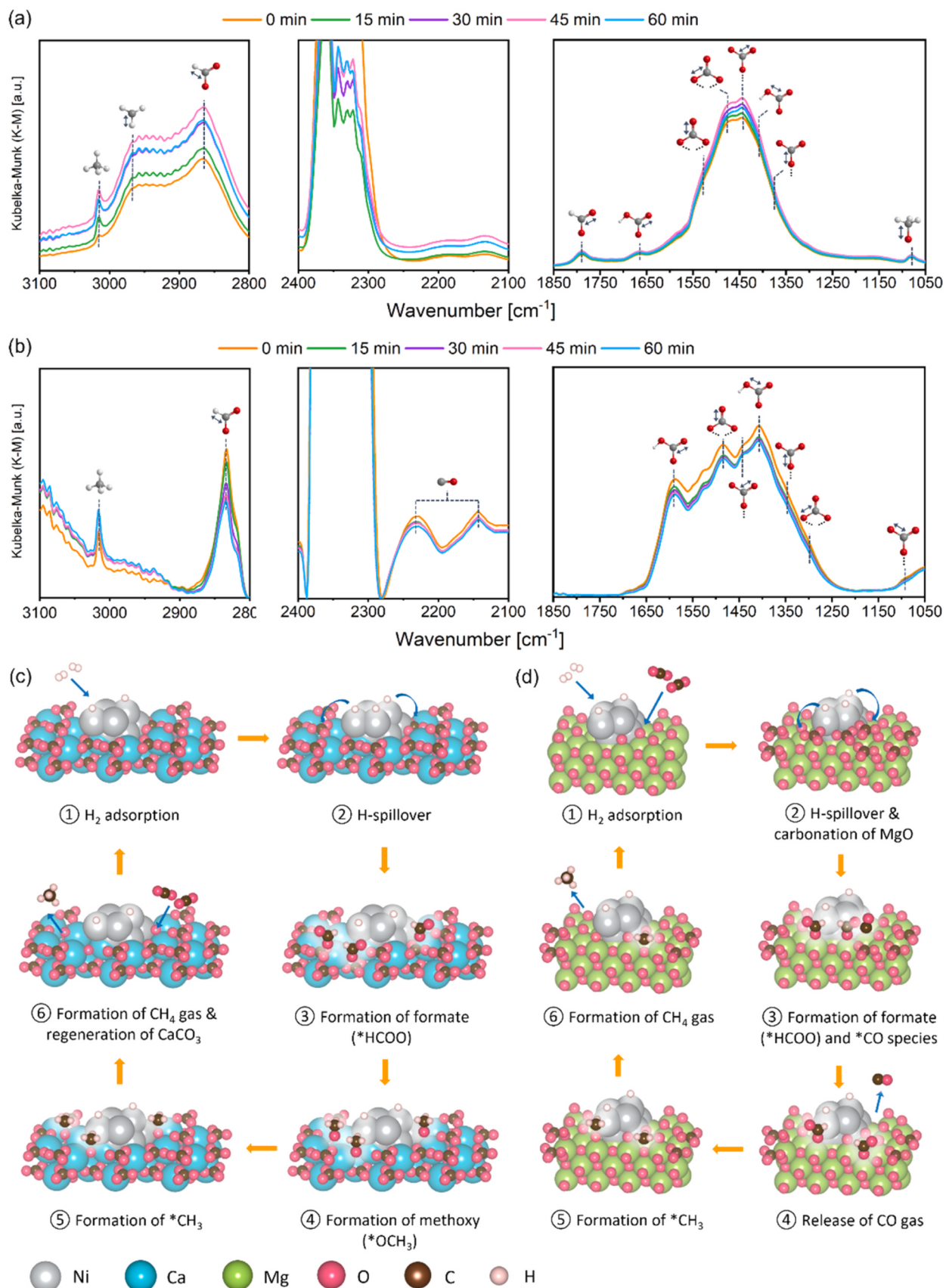


**Fig. 13.** in situ DRIFTS measurements on Ni/Ca (a) and Ni/Mg (b) at 400 °C under conventional  $\text{CO}_2$  hydrogenation conditions in 40 mL gas mixture of  $\text{CO}_2/\text{H}_2/\text{Ar}=5/20/15$  (i.e., co-feed  $\text{CO}_2$  and  $\text{H}_2$ ); (b) proposed reaction mechanism of conventional  $\text{CO}_2$  hydrogenation on (c) Ni/Ca and (d) Ni/Mg catalysts.

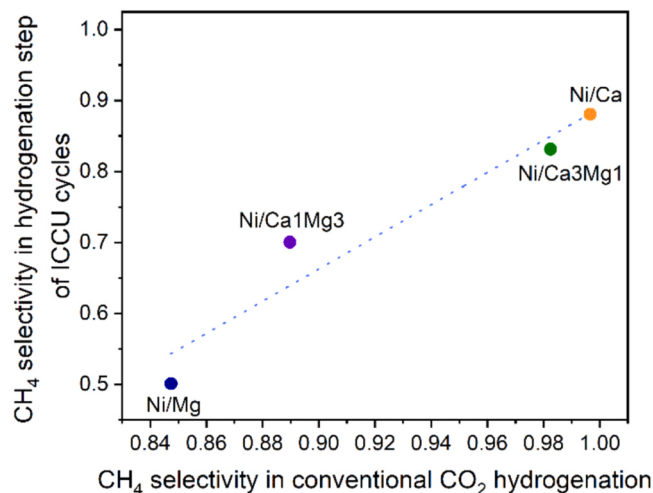


**Fig. 14.** Correlation between CH<sub>4</sub> selectivity between the direct hydrogenation step during ICCU cycles (10 vol% H<sub>2</sub>/N<sub>2</sub>, 400 °C) and conventional CO<sub>2</sub> hydrogenation with co-feed of CO<sub>2</sub> and H<sub>2</sub> (H<sub>2</sub>/CO<sub>2</sub>=4/1, 350 °C) for the various DFM formulations.

structure, CO<sub>2</sub> capture performance and catalytic performance of Ni/Ca remains stable, affording a cyclic CH<sub>4</sub> yield of approximately 1.25 mmol/g with a CH<sub>4</sub> selectivity of near-unity, while both surface carbonate and bulk carbonate participate in the reaction, with the former proceeds at notably faster rates. The superior performance of Ni/Ca DFM could be attributed to it having sufficient moderate and strong basic sites (as characterised by CO<sub>2</sub>-TPD), as well as the unique metal-support interaction across the Ni/CaCO<sub>3</sub> interface (as characterised by H<sub>2</sub>-TPR) that favours the hydrogenation of carbonates via the formate pathway.

Lastly, we report a strong correlation between the reaction mechanism and product selectivity of the ICCU cycles and those of conventional CO<sub>2</sub> hydrogenation; this correlation could be exploited for elucidating catalytic mechanisms for the hydrogenation of immobilised CO<sub>2</sub> or carbonate.

#### CRediT authorship contribution statement

**Xianyue Wu:** Formal analysis, Investigation, Visualization, Writing – original draft. **Ribooga Chang:** Formal analysis, Investigation. **Mingwu Tan:** Investigation. **Longgang Tao:** Investigation. **Qianwenhao Fan:** Investigation. **Xiaochun Hu:** Investigation. **Hui Ling Tan:** Investigation. **Michelle Åhlén:** Investigation. **Ocean Cheung:** Conceptualization, Writing – review & editing, Supervision. **Wen Liu:** Conceptualization, Writing – review & editing, Supervision.

#### Declaration of Competing Interest

The authors declare that they have no known competing financial interests or personal relationships that could have appeared to influence the work reported in this paper.

#### Data Availability

Data will be made available on request.

#### Acknowledgements

The authors thank the financial support by National Research Foundation of Singapore under its Campus for Research Excellence and Technological Enterprise (CREATE) scheme, the Swedish Research Council (VR, Grant no. 2020-04029), and the Swedish Foundation for

International Cooperation in Research and Higher Education (STINT, Grant No IB2019-8184).

#### Appendix A. Supporting information

Supplementary data associated with this article can be found in the online version at doi:10.1016/j.apcatb.2023.123053.

#### References

- [1] IEA. Global Energy Review: CO<sub>2</sub> Emissions in 2020, 2021.
- [2] IEA. CO<sub>2</sub> Emissions in 2022, <<https://www.iea.org/reports/co2-emissions-in-2022>> (2023).
- [3] Chu, J. Short-lived greenhouse gases cause centuries of sea-level rise, <<https://climate.nasa.gov/news/2533/short-lived-greenhouse-gases-cause-centuries-of-sea-level-rise/>> (2017).
- [4] Mebrahtu, C. et al. in Studies in Surface Science and Catalysis Vol. 178 (eds Stefania Albonetti, Siglinda Perathoner, & Elsie Alessandra Quadrelli) 85–103 (Elsevier, 2019).
- [5] P. Pall, et al., Anthropogenic greenhouse gas contribution to flood risk in England and Wales in autumn 2000, Nature 470 (2011) 382–385, <https://doi.org/10.1038/nature09762>.
- [6] A.W. Zimmermann, et al., Techno-economic assessment guidelines for CO<sub>2</sub> utilization, Front. Energy Res. 8 (2020), <https://doi.org/10.3389/fenrg.2020.00005>.
- [7] M. Finkenrath, Carbon dioxide capture from power generation - status of cost and performance, Chem. Eng. Technol. 35 (2012) 482–488, <https://doi.org/10.1002/ceat.201100444>.
- [8] R. Banerjee, et al., High-throughput synthesis of zeolitic imidazolate frameworks and application to CO<sub>2</sub> capture, Science 319 (2008) 939–943, <https://doi.org/10.1126/science.1152516>.
- [9] S. Kumar, R. Srivastava, J. Koh, Utilization of zeolites as CO<sub>2</sub> capturing agents: advances and future perspectives, J. CO<sub>2</sub> Util. 41 (2020), 101251, <https://doi.org/10.1016/j.jcou.2020.101251>.
- [10] J. Liao, B. Jin, Y. Zhao, Z. Liang, Highly efficient and durable metal-organic framework material derived Ca-based solid sorbents for CO<sub>2</sub> capture, Chem. Eng. J. 372 (2019) 1028–1037, <https://doi.org/10.1016/j.cej.2019.04.212>.
- [11] W. Liang, et al., A tailor-made interpenetrated MOF with exceptional carbon-capture performance from flue gas, Chem. 5 (2019) 950–963, <https://doi.org/10.1016/j.chempr.2019.02.007>.
- [12] M.T. Dunstan, et al., Large scale computational screening and experimental discovery of novel materials for high temperature CO<sub>2</sub> capture, Energy Environ. Sci. 9 (2016) 1346–1360, <https://doi.org/10.1039/C5EE03253A>.
- [13] B. Arias, M. Alonso, C. Abanades, CO<sub>2</sub> capture by calcium looping at relevant conditions for cement plants: experimental testing in a 30 kWthPilot plant, Ind. Eng. Chem. Res. 56 (2017) 2634–2640, <https://doi.org/10.1021/acs.iecr.6b04617>.
- [14] M. Erans, M. Jeremias, V. Manovic, E.J. Anthony, Operation of a 25 KWth calcium looping pilot-plant with high oxygen concentrations in the calciner, J. Vis. Exp. 128 (2017), e56122.
- [15] Y. Hu, Y. Guo, J. Sun, H. Li, W. Liu, Progress in MgO sorbents for cyclic CO<sub>2</sub> capture: a comprehensive review, J. Mater. Chem. A 7 (2019) 20103–20120, <https://doi.org/10.1039/C9TA06930E>.
- [16] C. Jeong-Potter, et al., Dual function materials (Ru+Na<sub>2</sub>O/Al2O3) for direct air capture of CO<sub>2</sub> and in situ catalytic methanation: The impact of realistic ambient conditions, Appl. Catal. B: Environ. 307 (2022), 120990, <https://doi.org/10.1016/j.apcatb.2021.120990>.
- [17] A. Bermejo-López, B. Pereda-Ayo, J.A. González-Marcos, J.R. González-Velasco, Alternate cycles of CO<sub>2</sub> storage and in situ hydrogenation to CH<sub>4</sub> on Ni-Na2CO<sub>3</sub>/Al2O3: influence of promoter addition and calcination temperature, Sustain. Energy Fuels 5 (2021) 1194–1210, <https://doi.org/10.1039/D0SE01677B>.
- [18] A. Bermejo-López, B. Pereda-Ayo, J.A. Onrubia-Calvo, J.A. González-Marcos, J. R. González-Velasco, Tuning basicity of dual function materials widens operation temperature window for efficient CO<sub>2</sub> adsorption and hydrogenation to CH<sub>4</sub>, J. CO<sub>2</sub> Util. 58 (2022), 101922, <https://doi.org/10.1016/j.jcou.2022.101922>.
- [19] S. Cimino, R. Russo, L. Lisi, Insights into the cyclic CO<sub>2</sub> capture and catalytic methanation over highly performing Li-Ru/Al2O3 dual function materials, Chem. Eng. J. 428 (2022), 131275, <https://doi.org/10.1016/j.cej.2021.131275>.
- [20] R. Chang, X. Wu, O. Cheung, W. Liu, Synthetic solid oxide sorbents for CO<sub>2</sub> capture: state-of-the-art and future perspectives, J. Mater. Chem. A (2022), <https://doi.org/10.1039/DITA07697C>.
- [21] J.G. Jang, G.M. Kim, H.J. Kim, H.K. Lee, Review on recent advances in CO<sub>2</sub> utilization and sequestration technologies in cement-based materials, Constr. Build. Mater. 127 (2016) 762–773, <https://doi.org/10.1016/j.conbuildmat.2016.10.017>.
- [22] S. Valluri, V. Claremboux, S. Kawatra, Opportunities and challenges in CO<sub>2</sub> utilization, J. Environ. Sci. 113 (2022) 322–344, <https://doi.org/10.1016/j.jes.2021.05.043>.
- [23] V.A. Kuuskraa, M.L. Godec, P. Dipietro, CO<sub>2</sub> utilization from “next generation” CO<sub>2</sub> enhanced oil recovery technology, Energy Procedia 37 (2013) 6854–6866, <https://doi.org/10.1016/j.egypro.2013.06.618>.
- [24] C.-H. Huang, C.-S. Tan, A review: CO<sub>2</sub> utilization, Aerosol Air Qual. Res. 14 (2014) 480–499, <https://doi.org/10.4209/aaqr.2013.10.0326>.

[25] M.D. Burkart, N. Hazari, C.L. Twy, E.L. Zeitler, Opportunities and challenges for catalysis in carbon dioxide utilization, *ACS Catal.* 9 (2019) 7937–7956, <https://doi.org/10.1021/acscatal.9b02113>.

[26] M. Noussan, P.P. Raimondi, R. Scita, M. Hafner, The role of green and blue hydrogen in the energy transition—a technological and geopolitical perspective, *Sustainability* 13 (2021) 298.

[27] W. Li, et al., A short review of recent advances in CO<sub>2</sub> hydrogenation to hydrocarbons over heterogeneous catalysts, *RSC Adv.* 8 (2018) 7651–7669, <https://doi.org/10.1039/C7RA13546G>.

[28] R. Daiyan, I. MacGill, R. Amal, Opportunities and challenges for renewable power-to-X, *ACS Energy Lett.* 5 (2020) 3843–3847, <https://doi.org/10.1021/acsenergylett.0c02249>.

[29] L.-P. Merkouri, T.R. Reina, M.S. Duyar, Closing the carbon cycle with dual function materials, *Energy Fuels* 35 (2021) 19859–19880, <https://doi.org/10.1021/acs.energyfuels.1c02729>.

[30] S. Sun, H. Sun, P.T. Williams, C. Wu, Recent advances in integrated CO<sub>2</sub> capture and utilization: a review, *Sustain. Energy Fuels* 5 (2021) 4546–4559, <https://doi.org/10.1039/D1SE00797A>.

[31] M. Noussan, P.P. Raimondi, R. Scita, M. Hafner, The role of green and blue hydrogen in the energy transition—a technological and geopolitical perspective, *Sustainability* 13 (2020) 1–26.

[32] Foreman, D. Is The World About To See An Oil Shortage?, <<https://www.api.org/news-policy-and-issues/blog/2021/02/24/is-the-world-about-to-see-an-oil-shortage>> (2021).

[33] M.S. Duyar, S. Wang, M.A. Arellano-Treviño, R.J. Farrauto, CO<sub>2</sub> utilization with a novel dual function material (DFM) for capture and catalytic conversion to synthetic natural gas: an update, *J. CO<sub>2</sub> Util.* 15 (2016) 65–71, <https://doi.org/10.1016/j.jcou.2016.05.003>.

[34] J. Chen, Y. Xu, P. Liao, H. Wang, H. Zhou, Recent progress in integrated CO<sub>2</sub> capture and conversion process using dual function materials: a state-of-the-art review, *Carbon Capture Sci. Technol.* 4 (2022), 100052, <https://doi.org/10.1016/j.ccst.2022.100052>.

[35] G. Liu, et al., Integrated CO<sub>2</sub> capture and utilisation: a promising step contributing to carbon neutrality, *Carbon Capture Sci. Technol.* 7 (2023), 100116, <https://doi.org/10.1016/j.ccst.2023.100116>.

[36] I.S. Omodolor, H.O. Otor, J.A. Andonegui, B.J. Allen, A.C. Alba-Rubio, Dual-Function Materials for CO<sub>2</sub> Capture and Conversion: A Review, *Ind. Eng. Chem. Res.* 59 (2020) 17612–17631, <https://doi.org/10.1021/acs.iecr.0c02218>.

[37] H. Sun, et al., Dual functional catalytic materials of Ni over Ce-modified CaO sorbents for integrated CO<sub>2</sub> capture and conversion, *Appl. Catal. B: Environ.* 244 (2019) 63–75, <https://doi.org/10.1016/j.apcatb.2018.11.040>.

[38] P. Panagiotopoulou, Hydrogenation of CO<sub>2</sub> over supported noble metal catalysts, *Appl. Catal. A: Gen.* 542 (2017) 63–70, <https://doi.org/10.1016/j.apcata.2017.05.026>.

[39] A. Karelovic, P. Ruiz, Mechanistic study of low temperature CO<sub>2</sub> methanation over Rh/TiO<sub>2</sub> catalysts, *J. Catal.* 301 (2013) 141–153, <https://doi.org/10.1016/j.jcat.2013.02.009>.

[40] M.A. Vannice, The catalytic synthesis of hydrocarbons from carbon monoxide and hydrogen, *Catal. Rev. Rev.* 14 (1976) 153–191, <https://doi.org/10.1080/03602457608073410>.

[41] A. Bermejo-López, B. Pereda-Ayo, J.A. González-Marcos, J.R. González-Velasco, Mechanism of the CO<sub>2</sub> storage and in situ hydrogenation to CH<sub>4</sub>. Temperature and adsorbent loading effects over Ru-CaO/Al2O3 and Ru-Na<sub>2</sub>CO<sub>3</sub>/Al2O3 catalysts, *Appl. Catal. B: Environ.* 256 (2019), 117845, <https://doi.org/10.1016/j.apcatb.2019.117845>.

[42] C. Jeong-Potter, et al., Aging study of low Ru loading dual function materials (DFM) for combined power plant effluent CO<sub>2</sub> capture and methanation, *Appl. Catal. B: Environ.* 310 (2022), 121294, <https://doi.org/10.1016/j.apcatb.2022.121294>.

[43] L. Proaño, et al., In-situ DRIFTS study of two-step CO<sub>2</sub> capture and catalytic methanation over Ru-Na<sub>2</sub>O/Al2O3 dual functional material, *Appl. Surf. Sci.* 479 (2019) 25–30, <https://doi.org/10.1016/j.apsusc.2019.01.281>.

[44] A. Loder, M. Siebenhofer, S. Lux, The reaction kinetics of CO<sub>2</sub> methanation on a bifunctional Ni/MgO catalyst, *J. Ind. Eng. Chem.* 85 (2020) 196–207, <https://doi.org/10.1016/j.jiec.2020.02.001>.

[45] A. Kurlov, A. Armutlulu, F. Donat, A.R. Studart, C.R. Müller, CaO-based CO<sub>2</sub> sorbents with a hierarchical porous structure made via microfluidic droplet templating, *Ind. Eng. Chem. Res.* 59 (2019) 7182–7188, <https://doi.org/10.1021/acs.iecr.9b05996>.

[46] G. Wang, et al., Ni-CaO dual function materials prepared by different synthetic modes for integrated CO<sub>2</sub> capture and conversion, *Chem. Eng. J.* 428 (2022), 132110, <https://doi.org/10.1016/j.cej.2021.132110>.

[47] L.R. Winter, et al., Elucidating the roles of metallic Ni and oxygen vacancies in CO<sub>2</sub> hydrogenation over Ni/CeO<sub>2</sub> using isotope exchange and in situ measurements, *Appl. Catal. B: Environ.* 245 (2019) 360–366, <https://doi.org/10.1016/j.apcatb.2018.12.069>.

[48] J. Ashok, M.L. Ang, S. Kawi, Enhanced activity of CO<sub>2</sub> methanation over Ni/CeO<sub>2</sub>-ZrO<sub>2</sub> catalysts: influence of preparation methods, *Catal. Today* 281 (2017) 304–311, <https://doi.org/10.1016/j.cattod.2016.07.020>.

[49] N. Rui, et al., Highly active Ni/CeO<sub>2</sub> catalyst for CO<sub>2</sub> methanation: preparation and characterization, *Appl. Catal. B: Environ.* 282 (2021), 119581, <https://doi.org/10.1016/j.apcatb.2020.119581>.

[50] P.K. de Bokx, R.L.C. Bonne, J.W. Geus, Strong metal-support interaction in Ni/TiO<sub>2</sub> catalysts: the origin of TiO<sub>x</sub> moieties on the surface of nickel particles, *Appl. Catal.* 30 (1987) 33–46, [https://doi.org/10.1016/S0166-9834\(00\)81009-X](https://doi.org/10.1016/S0166-9834(00)81009-X).

[51] Z. Zhang, L. Zhang, M.J. Hulse, N. Yan, Zirconia phase effect in Pd/ZrO<sub>2</sub> catalyzed CO<sub>2</sub> hydrogenation into formate, *Mol. Catal.* 475 (2019), 110461, <https://doi.org/10.1016/j.mcat.2019.110461>.

[52] M. Yamasaki, H. Habazaki, K. Asami, K. Izumiya, K. Hashimoto, Effect of tetragonal ZrO<sub>2</sub> on the catalytic activity of Ni/ZrO<sub>2</sub> catalyst prepared from amorphous Ni-Zr alloys, *Catal. Commun.* 7 (2006) 24–28, <https://doi.org/10.1016/j.catcom.2005.08.005>.

[53] K. Zhao, W. Wang, Z. Li, Highly efficient Ni/ZrO<sub>2</sub> catalysts prepared via combustion method for CO<sub>2</sub> methanation, *J. CO<sub>2</sub> Util.* 16 (2016) 236–244, <https://doi.org/10.1016/j.jcou.2016.07.010>.

[54] R.-P. Ye, et al., Enhanced stability of Ni/SiO<sub>2</sub> catalyst for CO<sub>2</sub> methanation: Derived from nickel phyllosilicate with strong metal-support interactions, *Energy* 188 (2019), 116059, <https://doi.org/10.1016/j.energy.2019.116059>.

[55] T. Pu, et al., Formation and influence of surface hydroxyls on product selectivity during CO<sub>2</sub> hydrogenation by Ni/SiO<sub>2</sub> catalysts, *J. Catal.* 400 (2021) 228–233, <https://doi.org/10.1016/j.jcat.2021.06.008>.

[56] R.-Y. Chein, C.-C. Wang, Experimental study on CO<sub>2</sub> methanation over Ni/Al<sub>2</sub>O<sub>3</sub>, Ru/Al<sub>2</sub>O<sub>3</sub>, and Ru-Ni/Al<sub>2</sub>O<sub>3</sub> catalysts, *Catalysts* 10 (2020) 1112.

[57] J. Sehested, J.A.P. Gelten, S. Helweg, Sintering of nickel catalysts: effects of time, atmosphere, temperature, nickel-carrier interactions, and dopants, *Appl. Catal. A: Gen.* 309 (2006) 237–246, <https://doi.org/10.1016/j.apcata.2006.05.017>.

[58] A.E. Aksoylu, A.N. Akin, Z.I. Önsan, D.L. Trimm, Structure/activity relationships in coprecipitated nickel-alumina catalysts using CO<sub>2</sub> adsorption and methanation, *Appl. Catal. A: Gen.* 145 (1996) 185–193, [https://doi.org/10.1016/0926-860X\(96\)00143-3](https://doi.org/10.1016/0926-860X(96)00143-3).

[59] L.-P. Merkouri, et al., Flexible NiRu systems for CO<sub>2</sub> methanation: from efficient catalysts to advanced dual-function materials, *Nanomaterials* 13 (2023) 506.

[60] L.-P. Merkouri, T. Ramirez Reina, M.S. Duyar, Feasibility of switchable dual function materials as a flexible technology for CO<sub>2</sub> capture and utilisation and evidence of passive direct air capture, *Nanoscale* 14 (2022) 12620–12637, <https://doi.org/10.1039/DNR02688K>.

[61] L. Hu, A. Urakawa, Continuous CO<sub>2</sub> capture and reduction in one process: CO<sub>2</sub> methanation over unpromoted and promoted Ni/ZrO<sub>2</sub>, *J. CO<sub>2</sub> Util.* 25 (2018) 323–329, <https://doi.org/10.1016/j.jcou.2018.03.013>.

[62] L. Proaño, et al., Mechanistic assessment of dual function materials, composed of Ru-Ni, Na<sub>2</sub>O/Al<sub>2</sub>O<sub>3</sub> and Pt-Ni, Na<sub>2</sub>O/Al<sub>2</sub>O<sub>3</sub>, for CO<sub>2</sub> capture and methanation by in-situ DRIFTS, *Appl. Surf. Sci.* 533 (2020), 147469, <https://doi.org/10.1016/j.apsusc.2020.147469>.

[63] T. Sasayama, et al., Integrated CO<sub>2</sub> capture and selective conversion to syngas using transition-metal-free Na/Al<sub>2</sub>O<sub>3</sub> dual-function material, *J. CO<sub>2</sub> Util.* 60 (2022), 102049, <https://doi.org/10.1016/j.jcou.2022.102049>.

[64] H. Sun, et al., Integrated carbon capture and utilization: synergistic catalysis between highly dispersed Ni clusters and ceria oxygen vacancies, *Chem. Eng. J.* 437 (2022), 135394, <https://doi.org/10.1016/j.cej.2022.135394>.

[65] O. Cheung, et al., Nanostructure and pore size control of template-free synthesised mesoporous magnesium carbonate, *RSC Adv.* 6 (2016) 74241–74249, <https://doi.org/10.1039/C6RA14171D>.

[66] M. Vall, J. Hultberg, M. Strømme, O. Cheung, Inorganic carbonate composites as potential high temperature CO<sub>2</sub> sorbents with enhanced cycle stability, *RSC Adv.* 9 (2019) 20273–20280, <https://doi.org/10.1039/C9RA02843A>.

[67] R. Sun, et al., Amorphous calcium carbonate constructed from nanoparticle aggregates with unprecedented surface area and mesoporosity, *ACS Appl. Mater. Interfaces* 10 (2018) 21556–21564, <https://doi.org/10.1021/acsm.8b03939>.

[68] Y. Yu, et al., Alkaline-carbonate-templated carbon: effect of template nature on morphology, oxygen species and supercapacitor performances, *Appl. Surf. Sci.* 575 (2022), 151771, <https://doi.org/10.1016/j.apsusc.2021.151771>.

[69] K.S.P. Karunadasa, C.H. Manaratne, H.M.T.G.A. Pitawala, R.M.G. Rajapakse, Thermal decomposition of calcium carbonate (calcite polymorph) as examined by in-situ high-temperature X-ray powder diffraction, *J. Phys. Chem. Solids* 134 (2019) 21–28, <https://doi.org/10.1016/j.jpcs.2019.05.023>.

[70] D. Mahon, G. Claudio, P. Eames, An experimental study of the decomposition and carbonation of magnesium carbonate for medium temperature thermochemical energy storage, *Energies* 14 (2021) 1316.

[71] M.-H. Jao, C.-C. Cheng, C.-F. Lu, K.-C. Hsiao, W.-F. Su, Low temperature and rapid formation of high quality metal oxide thin film via a hydroxide-assisted energy conservation strategy, *J. Mater. Chem. C* 6 (2018) 9941–9949, <https://doi.org/10.1039/C8TC03544J>.

[72] M.C. Biesinger, B.P. Payne, L.W.M. Lau, A. Gerson, R.S.C. Smart, X-ray photoelectron spectroscopic chemical state quantification of mixed nickel metal, oxide and hydroxide systems, *Surf. Interface Anal.* 41 (2009) 324–332, <https://doi.org/10.1002/sia.3026>.

[73] M.C. Biesinger, et al., Resolving surface chemical states in XPS analysis of first row transition metals, oxides and hydroxides: Cr, Mn, Fe, Co and Ni, *Appl. Surf. Sci.* 257 (2011) 2717–2730, <https://doi.org/10.1016/j.apsusc.2010.10.051>.

[74] J. Huang, W. Liu, Y. Yang, Phase interactions in Mg-Ni-Al-O oxygen carriers for chemical looping applications, *Chem. Eng. J.* 326 (2017) 470–476, <https://doi.org/10.1016/j.cej.2017.05.176>.

[75] T. Nakayama, N. Ichikuni, S. Sato, F. Nozaki, Ni/MgO catalyst prepared using citric acid for hydrogenation of carbon dioxide, *Appl. Catal. A: Gen.* 158 (1997) 185–199, [https://doi.org/10.1016/S0926-860X\(96\)00399-7](https://doi.org/10.1016/S0926-860X(96)00399-7).

[76] J. Hu, P. Hongmanorom, V.V. Galvita, Z. Li, S. Kawi, Bifunctional Ni-Ca based material for integrated CO<sub>2</sub> capture and conversion via calcium-looping dry reforming, *Appl. Catal. B: Environ.* 284 (2021), 119734, <https://doi.org/10.1016/j.apcatb.2020.119734>.

[77] Q. Pan, J. Peng, T. Sun, S. Wang, S. Wang, Insight into the reaction route of CO<sub>2</sub> methanation: promotion effect of medium basic sites, *Catal. Commun.* 45 (2014) 74–78, <https://doi.org/10.1016/j.catcom.2013.10.034>.

[78] Y. Hu, et al., MxOy (M = Mg, Zr, La, Ce) modified Ni/CeO<sub>2</sub> dual functional materials for combined CO<sub>2</sub> capture and hydrogenation, *Int. J. Hydron. Energy* (2022), <https://doi.org/10.1016/j.ijhydene.2022.11.045>.

[79] J. Hu, P. Hongmanorom, P. Chirawatkul, S. Kawi, Efficient integration of CO<sub>2</sub> capture and conversion over a Ni supported CeO<sub>2</sub>-modified CaO microsphere at moderate temperature, *Chem. Eng. J.* 426 (2021), 130864, <https://doi.org/10.1016/j.cej.2021.130864>.

[80] A. Cárdenas-Arenas, et al., Isotopic and in situ DRIFTS study of the CO<sub>2</sub> methanation mechanism using Ni/CeO<sub>2</sub> and Ni/Al<sub>2</sub>O<sub>3</sub> catalysts, *Appl. Catal. B: Environ.* 265 (2020), 118538, <https://doi.org/10.1016/j.apcatb.2019.118538>.

[81] R.-P. Ye, et al., High-performance of nanostructured Ni/CeO<sub>2</sub> catalyst on CO<sub>2</sub> methanation, *Appl. Catal. B: Environ.* 268 (2020), 118474, <https://doi.org/10.1016/j.apcatb.2019.118474>.

[82] Y. Yu, et al., Enhanced performance and selectivity of CO<sub>2</sub> methanation over g-C<sub>3</sub>N<sub>4</sub> assisted synthesis of NiCeO<sub>2</sub> catalyst: Kinetics and DRIFTS studies, *Int. J. Hydron. Energy* 43 (2018) 15191–15204, <https://doi.org/10.1016/j.ijhydene.2018.06.090>.

[83] J. Zhang, Y. Yang, J. Liu, B. Xiong, Mechanistic understanding of CO<sub>2</sub> hydrogenation to methane over Ni/CeO<sub>2</sub> catalyst, *Appl. Surf. Sci.* 558 (2021), 149866, <https://doi.org/10.1016/j.apsusc.2021.149866>.

[84] S. Kattel, P. Liu, J.G. Chen, Tuning Selectivity of CO<sub>2</sub> Hydrogenation Reactions at the Metal/Oxide Interface, *J. Am. Chem. Soc.* 139 (2017) 9739–9754, <https://doi.org/10.1021/jacs.7b05362>.

[85] B. Yan, et al., Tuning CO<sub>2</sub> hydrogenation selectivity via metal-oxide interfacial sites, *J. Catal.* 374 (2019) 60–71, <https://doi.org/10.1016/j.jcat.2019.04.036>.

[86] X. Jia, X. Zhang, N. Rui, X. Hu, Liu C.-j, Structural effect of Ni/ZrO<sub>2</sub> catalyst on CO<sub>2</sub> methanation with enhanced activity, *Appl. Catal. B: Environ.* 244 (2019) 159–169, <https://doi.org/10.1016/j.apcatb.2018.11.024>.

[87] Y. Yan, et al., CO<sub>2</sub> hydrogenation to methanol on tungsten-doped Cu/CeO<sub>2</sub> catalysts, *Appl. Catal. B: Environ.* 306 (2022), 121098, <https://doi.org/10.1016/j.apcatb.2022.121098>.

[88] Y. Kim, et al., Highly CO-selective Ni-MgO–Ce<sub>x</sub>Zr<sub>1-x</sub>O<sub>2</sub> catalyst for efficient low-temperature reverse water-gas shift reaction, *J. Ind. Eng. Chem.* 118 (2023) 341–350, <https://doi.org/10.1016/j.jiec.2022.11.019>.